Statistics in Volcanology
Volume 3
August 18, 2017

Bayesian construction of a long-term vent opening map in the Long Valley volcanic region (CA, USA)

Andrea Bevilacqua[1]
Marcus Bursik[1]
Abani Patra[2]
E. Bruce Pitman[3]
Ryan Till[1]

(1) University at Buffalo, Department of Geology
(2) University at Buffalo, Department of Mechanical and Aerospace Engineering
(3) University at Buffalo, Department of Materials Design and Innovation

Keywords:
Vent opening probability maps, Long Valley volcanic region, Bayesian model averaging

Correspondence:
Andrea Bevilacqua: abevilac@buffalo.edu
University at Buffalo, Department of Geology, 126 Cooke Hall, 14260 Buffalo, NY (USA)

citation:
Bevilacqua, A., M. Bursik, A. Patra, E. B. Pitman, and R. Till (2017) Bayesian construction of a long-term vent opening map in the Long Valley volcanic region (CA, USA), *Statistics in Volcanology* 3.1 : 1 – 36. DOI: http://dx.doi.org/10.5038/2163-338X.3.1

Abstract

The Long Valley volcanic region is an active volcanic area situated at the eastern base of the Sierra Nevada escarpment and dominated by a 32 km wide resurgent caldera created ~760 ka. Eruptions after 180 ka have been localized at Mammoth Mountain on the western rim of the caldera and along the Mono-Inyo Craters volcanic chain stretching about 45 km northward. Three different probability models have been developed and then combined in a logic tree to estimate the long-term spatial probability of vent opening. These models include *(i)* an anisotropic kernel density estimator based on past vent locations, *(ii)* a new Bayesian model for coupling new vents with pre-existing faults, and *(iii)* a uniformly distributed probability map. The model combination procedure relies on Bayesian model averaging. Using a doubly stochastic framework enables us to incorporate some of the main sources of epistemic uncertainty about the interpretation of the volcanic system, thereby exploring their effect. Our vent-opening probability maps show two higher likelihood regions for new vent opening, one around Mammoth Mountain to the south, and the other along the Mono-Inyo Craters to the north. The spatial vent opening probability, conditional on an eruption, is estimated as ~64% in the northern region and ~36% in the southern region, with an uncertainty of about ±20%. These findings provide a rational basis for the hazard mapping of a potential eruption in the Long Valley volcanic region, suggesting that the hazard associated with Mammoth Mountain volcanism should be fully evaluated.

Introduction

The Long Valley volcanic region (LVVR) is an area of bimodal basaltic-rhyolitic volcanism encompassing ~4000 km^2, which became active at ~4 Ma as the Sierran microplate started to detach from North America (*Hildreth*, 2004). It is dominated by the 32 km by 18 km wide, resurgent Long Valley caldera, which formed ~760 ka during the eruption of the Bishop Tuff. Recent activity, including vents that were active after 180 ka, are associated with the Mammoth Mountain vent system, including a composite dome volcano at its core on the southwest topographic rim of the caldera, and the Mono-Inyo Craters volcanic chain and Mono Lake islands, a nearly linear array of vents stretching north of the caldera for ~45 km (Figure 1).

Although activity in the Mammoth Mountain system started as early as ~230 ka (*Hildreth et al.*, 2014), current evidence traces initiation of the Mono-Inyo Craters and Mono Lake islands systems back only to ~60 ka. Both systems were active in the Holocene, with the most recent magmatic eruptions occurring at ~9 ka (*Browne et al.*, 2010) from the Mammoth Mountain system, and at ~0.3 ka (*Bursik & Sieh*, 2013) from the Mono-Inyo/Mono Lake islands systems. The hazard assessment for the LVVR (*Miller et al.*, 1982) does not include an evaluation of the potential for a future eruption at Mammoth Mountain, but recent mapping, geochronologic and petrologic studies, as well as geophysical unrest, suggest that the Mammoth Mountain system is potentially active (*Hill*, 2006; *Hildreth et al.*, 2014; *Peacock et al.*, 2016). Furthermore, Mammoth Mountain is the focus of continuing diffuse, magmatic CO_2 degassing (*e.g., Farrar et al.*, 1995; *McGee & Gerlach*, 1998; *Gerlach et al.*, 1999). A principal source of uncertainty affecting spatial forecasts is the relevance of past Mammoth Mountain activity to future activity – is a vent likely to form again in this area in the future? Zones that have not seen magmatism for some time, but were active during the recent past, such as zones around Mammoth Mountain, may be *volcanic gaps* where crustal extension must again be accommodated, leading to possible future dike injection and eruptions (see, *e.g., Bursik & Sieh*, 1989; *Bursik*, 2009).

Evaluating the potential for an eruption from the Mammoth Mountain system depends on a number of factors. Pre-existing faults are often associated with the opening of new vents and typically represent a weakness element that may favor and deviate magma ascent and eruption (*Connor et al.*, 2000; *Calais et al.*, 2008), especially in a region where the link between tectonism and volcanism is strong, such as the LVVR. A key issue is therefore the distance from a fault outcrop at which an increased probability of vent opening could be expected. Other factors, including the strike and dip of the fault and the magma pressure and depth of interaction, could also be relevant (*Gaffney et al.*, 2007; *Le Corvec et al.*, 2013).

Especially important to the potential for volcanic hazards in the LVVR is the identification of likely locations of future vents. This is a key component of volcanic hazard and risk assessment, given the wide dispersion of eruptive locations within caldera systems and volcanic fields (*Woo*, 1999; *Mader et al.*, 2006; *Rougier et al.*, 2013). A map of the potential

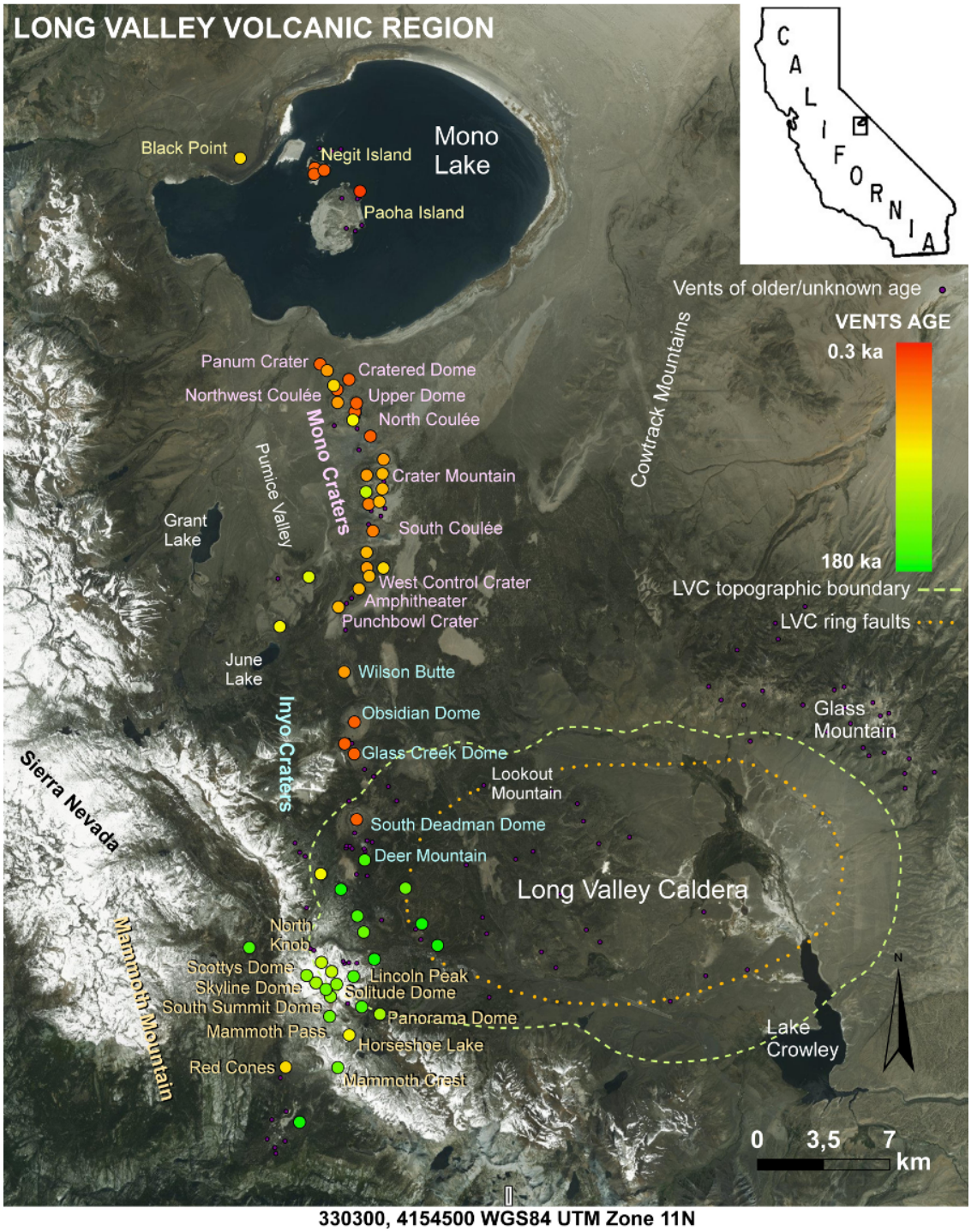

Figure 1: LVVR and the locations of past vents. Vent locations active after 180 ka are colored from green to yellow to red based on their age (also see the worksheet found in the additional file, `TableS1.xlsx`). Spatial groups of vents are labeled and also color coded. The Long Valley caldera topographic boundary and ring faults are outlined with dashed lines (from *Bailey*, 1989; *Hildreth*, 2004).

for vent opening displays the estimated probability of a vent opening per km^2 at each point within a region of interest (*e.g., Connor & Hill*, 1995; *Marti & Felpeto*, 2010; *Bebbington & Cronin*, 2011; *Connor et al.*, 2012; *Cappello et al.*, 2012; *Bartolini et al.*, 2013; *Selva et al.*, 2012; *Bevilacqua et al.*, 2015). Different strands of data can be used and various modeling choices can be made in developing a vent opening map. Multiple procedures appear to be reasonable and have been successfully adopted. Many are based on bivariate kernel density estimation, but differ in specifics. A nearest neighbor approach (*Connor & Hill*, 1995), plug-in bandwidth matrix selection (*Duong & Hazelton*, 2003), cross-validation bandwidth selection (*Duong*, 2007), and Kullback-Leibler score (*Vere-Jones*, 1992) have all been used, some in the geophysical setting (*Bebbington*, 2015). These techniques are spatial, although time can be taken into consideration separately (*Bebbington*, 2013), and one spatio-temporal model has been constructed (*Connor & Hill*, 1995). None of these models, however, explicitly incorporate the potential *jumping* of activity in a volcanic gap filling sequence of eruptions.

In this study we focus on a spatial assessment; the probability of vent opening is conditioned on the occurrence of a new eruption in the foreseeable future, and the estimates of vent opening do not have an associated temporal window. We will provide long-term assessments, based on the record of past eruptions and on volcanic and structural features of the region, without including any short-term (monitoring-based) information (*Marzocchi & Bebbington*, 2012). Such long-term vent opening forecasts will help constrain the *next generation* of volcanic hazard zone maps, from which will stem improved understanding of societal vulnerability to volcano hazards, more targeted hazard mitigation strategies, and wise community growth and development planning. Moreover, we believe such long-term assessment provides the starting point for immediate hazard assessments based on the incorporation of geophysical monitoring data into the forecast (*Marzocchi et al.*, 2004; *Hincks et al.*, 2014; *Aspinall & Woo*, 2014).

We present a simple approach that integrates several models, with weights related to hind-casting performance (*i.e.* the *forecasting* of past events based on pre-existing data). This new multi-model approach linearly combines three possible models inside a probability mixture. Bayesian Model Averaging (BMA) is adopted for estimating the weight of each model (weights reflect the probability of a particular model being the most appropriate) (*e.g., Hoeting et al.*, 1999; *Ajami et al.*, 2007; *Steel*, 2011; *Yan & Moradkhani*, 2016). The models include elements of novelty, including the use of a different procedure for estimating the bandwidth and drift in a kernel density estimator (Model 1), and the use of a Bayesian method to add susceptibility around fault outcrops locations (Model 2). Moreover, the models expressly cope with the uncertainty affecting a possible shift of eruptive focus, and with sources of uncertainty related to tectonic data. In particular, we incorporate into our maps the available information from past vent location patterns, and tectonic structures, focusing specifically on some of the key epistemic uncertainties of the volcanic system.

Our method treats the volcano as a stochastic system that must be assessed with incomplete information and through careful interpretation of the uncertainty associated with each piece of information. For this reason the models are constructed, implicitly, as doubly stochastic (*e.g., Cox & Isham*, 1980; *Daley & Vere-Jones*, 2005, 2008; *Jaquet et al.*, 2008, 2012). This means that the statistical distribution of the location of the next eruptive vent is represented using ill-constrained parameters. These parameters are treated as random variables (*e.g., Bevilacqua et al.*, 2015, 2016; *Neri et al.*, 2015; *Bevilacqua*, 2016). We define two different probability measures, one that describes the physical variability of the system (*aleatory* uncertainty), and the second representing the *epistemic* uncertainty due to imperfect knowledge of the system under study (*Sparks & Aspinall*, 2004; *Marzocchi & Bebbington*, 2012). This division corresponds to the distinction between an intrinsic randomness of the system and the additional uncertainty that affects its representation, the latter originating from incomplete information and expressing the degree of belief in alternative assumptions. As a consequence of this approach, map values will have their own confidence intervals (*e.g., Selva et al.*, 2012; *Bevilacqua et al.*, 2015).

This study is structured as follows. First, the LVVR is described. Second, the volcanic datasets (past vent locations and ages, tectonic structures) are presented. Third, the implementation of the main uncertainty sources and details of the statistical models are given. Fourth, the vent opening probability maps, with uncertainty quantification, are presented and discussed.

1 Long Valley volcanic region

The LVVR is located at the western edge of California, along the Sierra Nevada frontal fault escarpment. It includes Long Valley caldera (LVC), an oval depression 32 km wide in the E-W direction and 18 km in the N-S direction, and the

Mono-Inyo Craters volcanic chain, which extends 45 km from the west edge of the caldera to Mono Lake (*Bailey*, 1989), (*Bursik & Sieh*, 2013). Mammoth Mountain is a 3400 m high lava dome complex on the southwestern edge of the caldera, rising about 1000 m above it (*Hildreth et al.*, 2014; *Hildreth & Fierstein*, 2016, Figure 1).

Mono Craters are the northern part of the Mono-Inyo Craters volcanic chain. These craters form a 17 km long ridge composed of more than 30 overlapping volcanic domes and craters, rising 610 m above the surrounding terrain (*Bursik & Sieh*, 1989). Inyo Craters form a less prominent line of volcanic domes and craters extending 10 km south of the Mono Craters into the western boundary of LVC (*Miller*, 1985).

Volcanism in the region began before 3 Ma (*Hildreth*, 2004). The most voluminous and explosive eruption, which caused the subsidence that formed the LVC occurred ~760 ka, with the eruption of ~600 km^3 of rhyolitic magma and the deposition of the widespread Bishop Tuff. The deposit thickness is locally 200 m in the Upper Owens Valley and reaches 1500 m inside the caldera (*Bailey*, 1976; *Hildreth & Mahood*, 1986). Today the caldera floor ranges in elevation from 2000 masl in the mostly barren eastern half to about 2600 masl in its western half, which is hilly and mostly forested. Topographic walls of the caldera rise 3000−3600 masl in elevation, except on the east and southeast sides, where the rim is only 100−200 m above the surrounding terrain. A 10 km wide, 500 m high resurgent dome formed in the central part of the caldera floor. Between the central hills and the caldera walls is an annular depression referred to as the caldera moat.

The most recent activity in the LVVR after ~60 ka, issued from the volcanoes of Mono Lake, the Mono-Inyo Craters, some small eruptions in the Mammoth Mountain periphery, and the phreatic explosion pits of Mammoth Mountain (*Sieh & Bursik*, 1986; *Bursik & Sieh*, 2013). The details of eruptions younger than 1000 years are relatively well known, progressing from an explosive sub-plinian phase through a surge and pyroclastic flow phase, to a debris flow and dome building phase. Older events are often discovered by examining deposits found in distal outcrops, although relationships between the outcrops and source vents generally remain uncertain (*Bursik et al.*, 2014; *Yang & Bursik*, 2016). Past activity includes an ~1 km^3 eruption in 1325−1350 AD along a 25 km section of the Mono-Inyo Craters chain (*Sieh & Bursik*, 1986). The most recent eruption, in ~1700 AD, created Paoha Island in Mono Lake (*Hildreth*, 2004).

Seismologic and magnetotelluric studies (*Achauer et al.*, 1986; *Peacock et al.*, 2015, 2016) suggest that numerous, separate, mid-crustal, potentially active magmatic sources (partial melt zones) lie in an irregular, but N-S elongated zone extending from Mono Lake to Mammoth Mountain.

The ongoing period of unrest in the LVVR started in 1978 with a magnitude 5.8 earthquake (*Hill*, 2006, 2017; *Hill et al.*, 2017). Monitoring studies recorded numerous episodes of increased unrest in the LVC and under Mammoth Mountain, including one in 2014 (*Prejean et al.*, 2003; *Shelly & Hill*, 2011; *Shelly et al.*, 2015). Diffuse CO_2 emissions at Mammoth Mountain claimed four lives in recent decades and killed ~40 km^2 of forest (*Farrar et al.*, 1995; *McGee & Gerlach*, 1998; *Gerlach et al.*, 1999). This long period of geophysical and geochemical unrest may culminate in a future volcanic eruption that could have a serious impact on the region. This makes probabilistic analysis of the location pattern of vents a timely and important task.

2 Dataset description

The inputs for the probabilistic maps consist of two different types of datasets: *(i)* the location and age of vent openings after 180 ka (*Bursik & Sieh*, 2013; *Hildreth et al.*, 2014; *Hildreth & Fierstein*, 2016), and *(ii)* the location of fault outcrops and their measured extension rate (*Bailey*, 1989; *Bursik & Sieh*, 1989). Data sources include new field work. Unless reported otherwise, the data are mapped on a regular grid of 200 × 200 cells, each cell is 500 × 500 m, with the lower left corner of the grid at (271050.1 E, 4134249 N) WGS84 UTM Zone 11N coordinates.

2.1 Distribution of past vents

The first dataset is the space-time location of 81 known past events after 180 ka (Figure 1 and the additional file, `TableS1.xlsx`). The selected time window contains events from the Mammoth Mountain region and the Mono-Inyo Craters, including the youngest lava dome eruptions in the western part of LVC. The LVVR includes additional foci

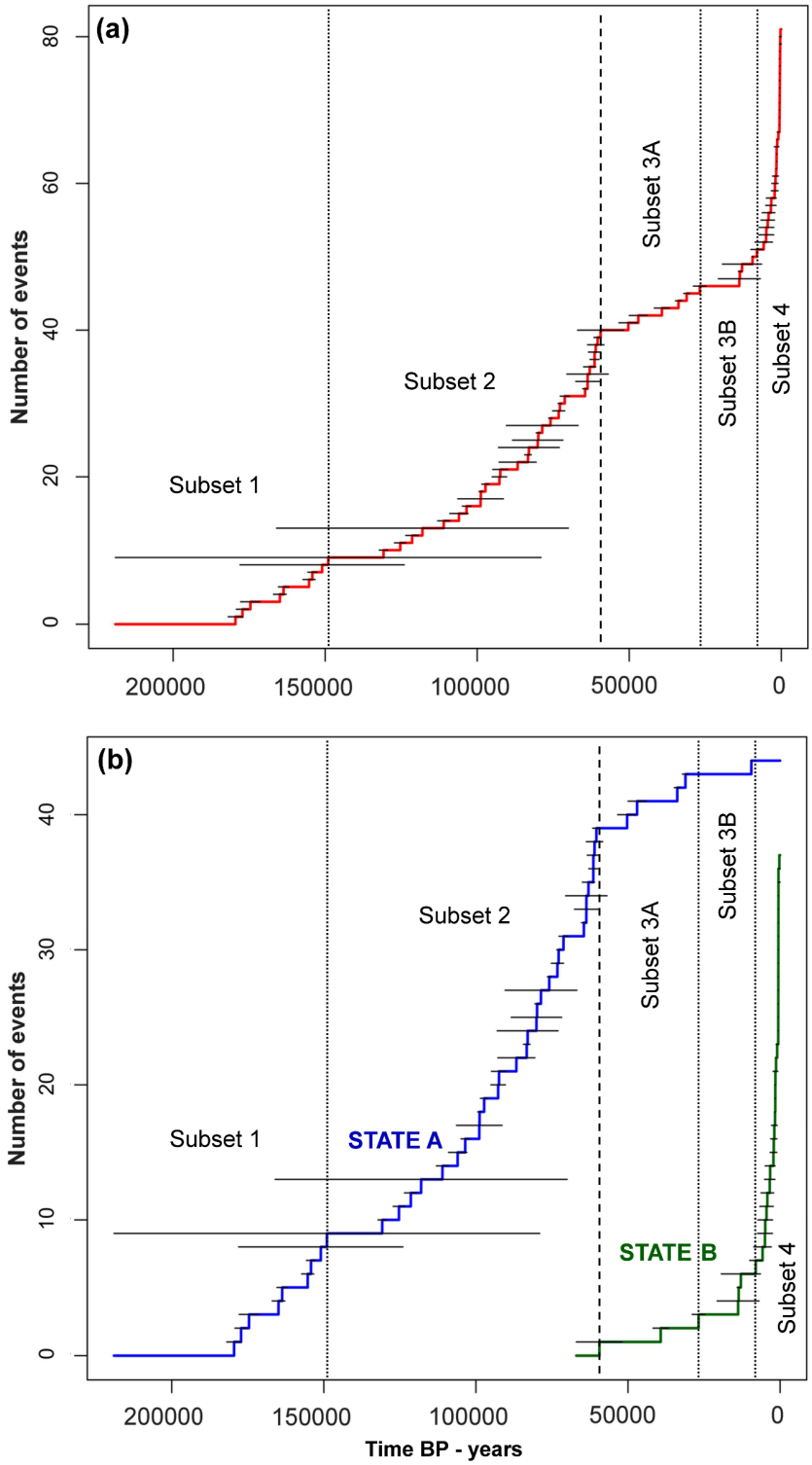

Figure 2: Cumulative number of past events as a function of time. Vertical lines separate subsets. (a) Red curve is the entire sequence. (b) Blue curve is State A; green curve is State B. Horizontal line segments display preliminary age uncertainty.

of activity beyond these sub-regions, but they are not included in the dataset because they are older and there are no signs of still un-crystallized magmatic reservoirs related to them. For each event, a spatial location is associated with an uncertainty uniformly distributed within a disk of 500 m radius —indeed most of the events left lava domes or craters. Each disk partially covers 4 to 9 grid cells. Because this spatial location uncertainty coincides with the cell size, it does not produce a large effect on the results, and we avoid carrying through the analysis additional spatial errors that might arise by using another grid size.

Most of the vents of unknown age, reported in Figure 1, occur among clusters of vents known to be older and are therefore outside of our temporal window. The other remaining vents that are not dated belong to the Mammoth or Mono systems and we neglected their effect on the statistical models. However, the presence of these vents must be acknowledged and additional field work may provide dates and thus, improve the overall accuracy of the estimates.

Preliminary age uncertainty, also displayed, is obtained by calibration of isotope dating and assuming a nominal 50% standard deviation error for obsidian hydration rind dating. Age uncertainty at LVVR is the subject of our ongoing research and it is not directly implemented in the model for vent opening location. An alternative eruption record is introduced in Appendix B), exploring the robustness of the results against the details of the temporal representation.

The vent location dataset assumes a one-to-one relationship between the eruptive sequence, often consisting of multiple pyroclastic events and dome formation, and the eruptive vent. The possible occurrence of eruptions with two or more simultaneously active vents in different sectors of the region is considered as two distinct events for the purpose of vent zonation, as is the possible occurrence of multiple eruption sequences from the same vent locality. For example, the North Mono eruption and the Inyo eruption, both of 1325-1350 AD, are considered as two separate events. Data locations and ages are derived from recent relevant literature (*Bursik & Sieh*, 2013; *Hildreth et al.*, 2014; *Hildreth & Fierstein*, 2016) and new field work.

Figure 2 shows the cumulative number of events as a function of time. This past record is divided into five subsets based on anomalously large shifts in spatial location or anomalous repose behavior:

Subset 1 180−149 ka, a 9-event sequence, average return time of ~3400 yr, concluded with an ~18 000 yr period of quiescence;

Subset 2 131−60 ka, a 30-event sequence, average return time of ~2350 yr, activity occurred in Mammoth Mountain area, concluded by a 20 km location shift to the first Mono event;

Subset 3A 59−27 ka, a 7-event sequence, average return time of ~4650 yr, a gradual shift of activity to Mono basin, concluded by an ~13 000 yr period of quiescence;

Subset 3B 14−8 ka, a 5-event sequence, average return time of ~1150 yr, main activity centered at Mono basin, concluded by a relative increase in activity rate;

Subset 4 < 6 ka, a 30-event sequence, average return time of ~200 yr, includes the most recent events and a much higher frequency, more than 10 vents were active simultaneously, 1325−1350 AD.

The ~20 km south to north shift in the locus of activity, which took place at ~60 ka, assumes great importance for the interpretation of the volcanic system, and corresponds to the activation of the northern part of the region. After 59−27 ka (Subset 3A, Figures 2 and 3), the eruption pattern showed a remarkable shift of the bulk of vent locations from the Mammoth Mountain region to Mono Basin. We remark that there is no evidence of eruptions from the Mono-Inyo system during the first 120 000 yr of the 180 ka record. Moreover, the physiography of Mono Basin does not allow for complete erosion or obliteration of volcanic structures in that time period, so the start of activity in the north at 60 ka is assumed to represent a real change in the vent opening pattern. For this reason, two different states of volcanic activity, named A and B, are considered for modeling the past vent locations, with a probability, p_1, of a new event occurring in State A. As the recent activity has been confined to State B, this would represent a change of state. The partition of the record into subsets has mostly a descriptive purpose, and does not play a role in the construction of probability models, except for the classification into State A or State B. Geographically, State A is related to the Mammoth Mountain area, and State B to the Mono Basin, with Inyo Craters lying in the middle. The UTM northing coordinate of the South Deadman vent (4175778 northing, WGS84 UTM Zone 11N) is adopted as the geographic divisor between State A and State B. State A mostly corresponds to the activity between 180 ka and 60 ka (Subsets 1−2, part of 3A and one event in 3B), while State B corresponds to the activity between 60 ka and the present time (part of Subset 3A, most of 3B and the entire

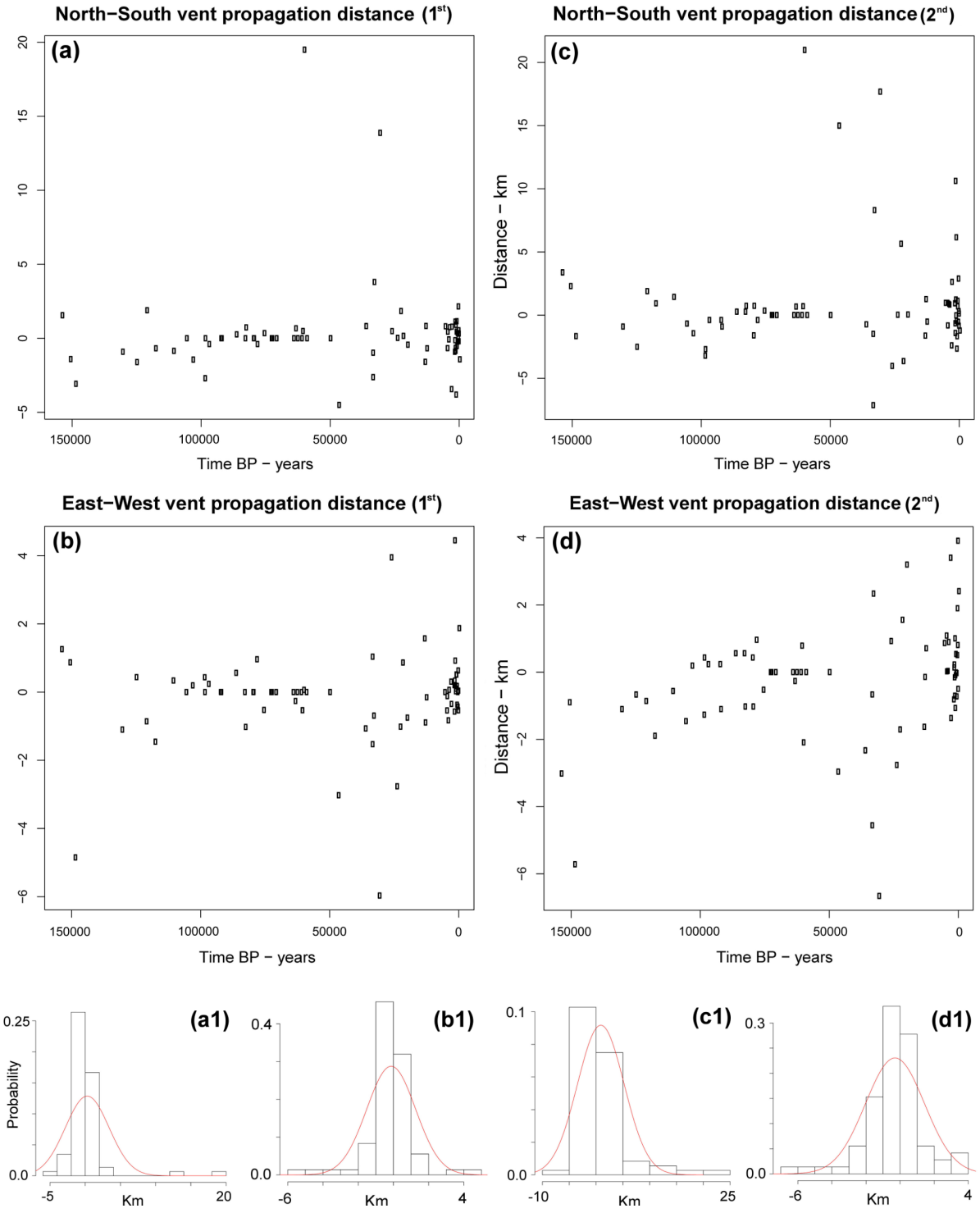

Figure 3: Time distribution of N−S **(a,c)** and E−W **(b,d)** vent propagation distances from 1st and 2nd spatially closest of pre-existing vents. Note, N−S scale **(a,c)** is ~5 times larger than E−W scale **(b,d)**. Histogram representations of the maximum likelihood Gaussian fits are shown in **a1−d1**.

Subset 4). The probability value of p_1 is difficult to estimate, due to the fact that the Mammoth Mountain system is partially crystallized, but since this volcanism is related to tectonics, reactivation of a current *volcanic gap* cannot be completely discounted. Moreover, most of the precursory signals picked up by the current monitoring activity come from the southern part of the volcanic region.

In general, the distance of propagation to each new vent from the set of previous vent locations is a quantitative parameter of major importance for describing the data (see also, *Magill et al.*, 2005). The temporal gap between eruptions is not used explicitly because of sometimes poor date control affecting possible vent ordering. For this reason, alternative distance measurements are defined, based on the distance of each new vent from the nearest of those previously active. Figure 3 shows the distribution of N−S and E−W propagation distances from the first and second spatially closest of the pre-existing vents after 180 ka. The 9 most ancient vents (Subset 1) are assumed as a starting dataset, necessary for defining the distance of propagation, and are not included in the plots. The data are well-represented by a Gaussian probability distribution according to the Shapiro-Wilk test (Figure 3, plots **a1**−**d1**). The vent propagation process is clearly anisotropic (*cf.,* Figure 3, plots **a, c** with plots **b, d**). It is worth mentioning that after the location shift took place, a significant increase in N−S propagation distances followed.

2.2 Distribution of faults

The second dataset adopted in this study concerns the fault locations and extension measurements in the region. The development of Long Valley volcanism is indeed related to the tectonic setting; the LVC lies in a releasing bend of the transtensional Walker Lane belt (*Bursik*, 2009; *Hill & Montgomery-Brown*, 2015). Much of the LVVR began down-dropping relative to the Sierra Nevada about 3 Ma, with a total differential motion of ~1100 m (*Huber*, 1981).

Pre-volcanic basement in the area is mainly Mesozoic granitic rock of the Sierra Nevada batholith, and Paleozoic meta-sedimentary and Mesozoic meta-volcanic rocks (*Bailey*, 1989). Structural and petrological studies in other regions show that some granitic plutons are emplaced in tectonic *holes*, pull-apart or extensional zones within regional strike-slip fault systems (*Vegas et al.*, 2001). If plutons develop in a local extensional tectonic environment, then it is natural to assume that the volcanoes above them will also form in relation to the tectonic environment. In particular, geological and geophysical evidence indicates that a tectonic pull apart zone or releasing bend guided the Bishop Tuff eruption and LVC subsidence (*Bursik*, 2009). Indeed, venting of the Bishop Tuff began near the intersection of the major regional faults and the caldera boundary (*Hildreth & Mahood*, 1986).

The Mono Basin is a northward plunging graben from the edge of LVC to Mono Lake (*Gilbert et al.*, 1968). The temporal pattern of offset rates suggests that the zone of greatest tectonic activity has migrated to the NW through time and now is focused on that area. The Mono Craters magma system has been considered to be forming in a releasing bend similar to LVC (*Bursik & Sieh*, 1989). In particular, the Mono magma chambers could enlarge by the incremental injection of dikes along one wall of the releasing bend, suppressing tectonic movement along the nearby range-front fault of the Sierra Nevada.

Two different sources of data are included in the analysis, four fault extension maps concerning Mono Basin, from *Bursik & Sieh* (1989), and a fault location map for the entire region, from *Bailey* (1989) (Figure 4). In the case of a lack of extension rate measurements for a particular structure, a value of 100 μm per year is assumed; this is a typical extension rate for faults in the region, and was adopted as a proxy for unknown extension rates in *Bursik & Sieh* (1989). A 100 m locational uncertainty buffer around fault scarps is assumed for producing the maps. These data are rasterized with 50 m accuracy, before being reduced to the final 500 m cell size of the vent opening probability maps.

The data available for the Mono Basin cover the faults that were active after 130 ka. In particular, they cover four time windows: 130 ka−66 ka, 66 ka−40 ka, 40 ka−14 ka, <14 ka. When considering the relevance of these data to vent opening, the younger fault slips, <14 ka, may be the only relevant dataset in a forecasting model. However, they are strongly correlated with dike accommodation beneath the Mono domes, and the older extension epochs could still be valuable data for the long-term tectonics of the region. Two different approaches are considered: one assumes only the most recent time window, the other picks up the maximum value of the extension rate from the three older time windows. The latter choice enables us to attenuate the weighting of the Mono dikes, but forces us to rely on the older, less accurate data.

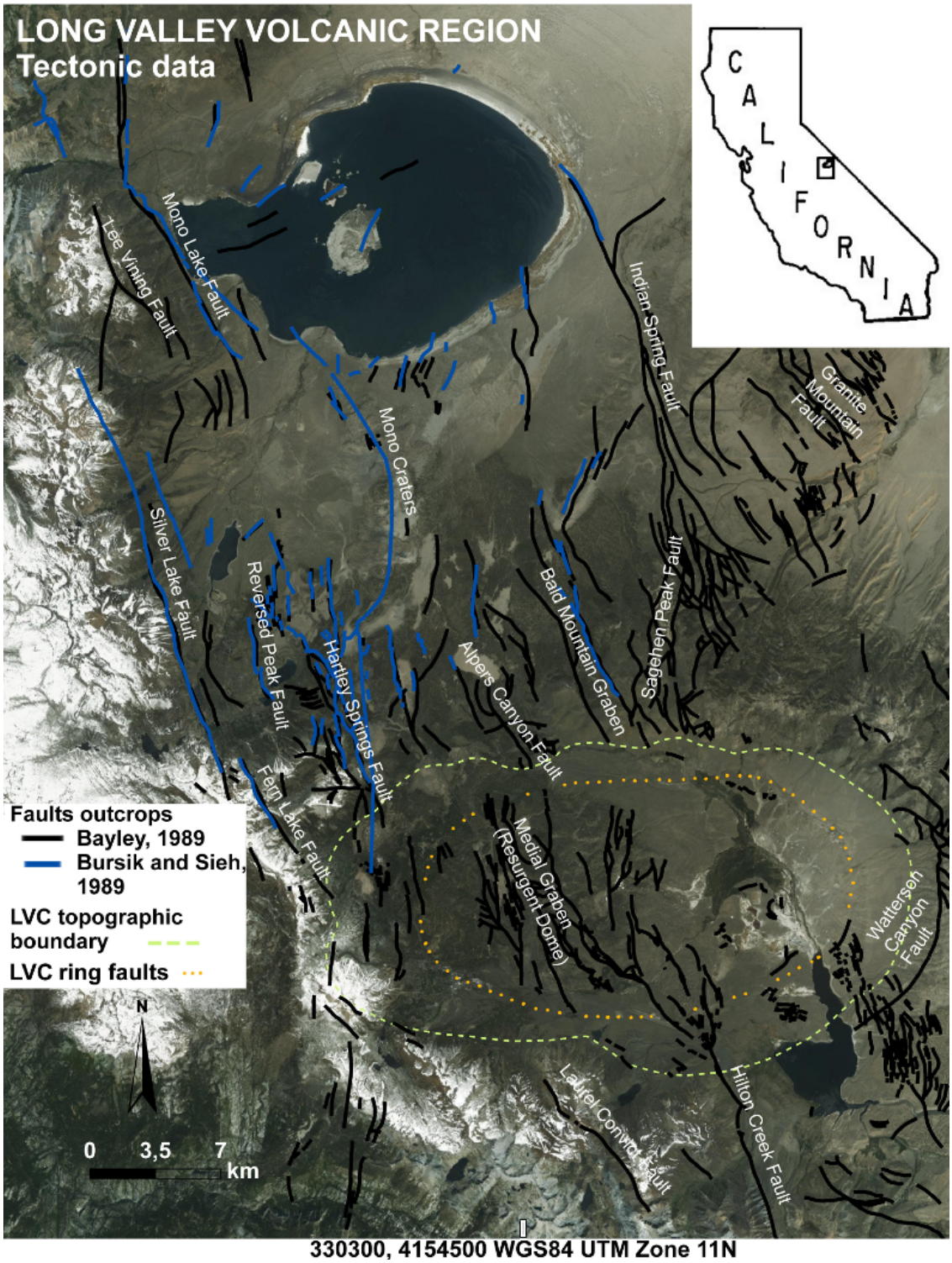

Figure 4: Long Valley volcanic region tectonic datasets. Fault outcrop locations are shown with colored lines and names. Different colors correspond to different sources: blue lines from *Bursik & Sieh* (1989), black lines from *Bailey* (1989). The Long Valley caldera topographic boundary and ring faults (*Hildreth*, 2004) are also displayed as a dashed line and a dotted line.

In general, a major component of the development of vent patterns is magma transport in dikes, mostly driven by the buoyancy of lighter magma in denser country rock. Analogue experiments, field observations and numerical modeling have been adopted for exploring the relative importance of the self-propagation of magma through pristine rock and the control exerted by pre-existing faults. For this reason, the outcrop pattern of faults can give precious information for the forecasting of future vent locations. Dike intrusion, like normal faulting, can accommodate extensional strain (*Bursik & Sieh*, 1989). Dike capture by a fault is primarily limited to steeply-dipping faults, except at the shallowest depths. This is because the pressure that the magma intrusion needs to exceed the normal stress across the fault walls generally increases with depth. If the wall stress is too high, then the dike propagates vertically, ignoring the fault. In addition, the fracture toughness of rock and the presence of pre-existing hanging wall fractures can influence the intrusion process (*Gaffney et al.*, 2007). Strike angle differences between dikes and faults can influence the interaction, as well as dike volume and the presence of multiple sub-parallel faults (*Le Corvec et al.*, 2013). The relationship between vent pattern and dike distribution is a complex geological problem and is the subject of much ongoing research (*Reches & Fink*, 1988; *Eichelberger et al.*, 1988; *Connor et al.*, 2000; *Gaffney & Damjanac*, 2006; *Kiyosugi et al.*, 2012; *Mazzarini et al.*, 2016).

A parameter of great importance in evaluating the complex relationship between faults and vents is the distance δ between the surficial fault outcrop and the past vent locations. Because the faults in the area can be considered to have, on average, a 60° dip (*Bursik & Sieh*, 1989), a first-order approximation for δ is given by half the depth of the shallowest fault-dike interaction. Two different bounds are considered for the depth 2δ: the ~10 km brittle-ductile transition of the crust in the region; and the ~2 km depth that is obtained from the numerical estimates of *Gaffney et al.* (2007) for a 60° fault dip, granite-like rock toughness, and short (0.1 m) pre-existing hanging wall fractures. While the first estimate might be overestimating the depth of possible interactions, the second estimate potentially underestimates the depth threshold, because the magma in any crustal chamber is likely to be more silicic than the basaltic magma assumed in the experiments.

3 Methods: doubly stochastic probability maps

The localization of the next eruptive vent in the LVVR is assumed to be a random variable, X, with a continuous density in the spatial domain. The unknown value of X is the geographical location of the next vent. A vent opening map is defined as the probability of a vent opening per km^2 at each point in the region of interest and can be displayed as a graph of the probability density of X per km^2. Most of the probability estimates have their own confidence intervals due to epistemic uncertainty, and even the final probability maps are affected by uncertainty; we calculate the mean, 5^{th} and 95^{th} percentile values for the vent opening probability density functions. We include the following uncertainty sources, modeled with the uncertainty parameters (p_i), where $i = 1, \ldots, 4$.

Separate alternative assessments of the Mammoth region (State A) and the Mono region (State B). The degree of belief in State A is p_1; the degree of belief in State B is $(1 - p_1)$. We choose to assume that a vent in the State A dataset does not count more than a vent in the State B dataset, without additional information. Hence, the random value of p_1 is uniformly sampled inside the interval $[0\% - 54\%]$, ($0.54 = 44/81$ is the proportion of past vents after 180 ka that opened in the Mammoth region). Specifically, we assume that the importance of vent locations belonging to the Mammoth Mountain region ranges from negligible to equally important with the vents in the more recently active Mono region. More detailed time-weighting of the two States, A and B, could be considered, but this weighting is affected by a proportional uncertainty. The Mono region started to be active at 60 ka, which accounts for only ~33% of the total time record duration, although the activity occurred during the most recent part of the record. Mammoth Mountain was active until ~10 ka, with only 4 events recorded at Mammoth Mountain after 60 ka, but its activity covers more than 90% of the duration of our record. In particular, after 10 ka more than 30 vents opened in the Mono region while none opened in the Mammoth region. A spatio-temporal nearest-neighbor analysis (e.g., *Connor & Hill*, 1995) would indicate a very low weight for the Mammoth region. In contrast, since 1980, geophysical precursory signals occurred in the Mammoth Mountain area, while almost none occurred in the Mono-Inyo Craters area (*Hill*, 2006; *Bergfeld et al.*, 2015). The p_1 range described above reasonably encompasses these contrasting strands of information. The two end members could be also described: *(i)* if $p_1 = 0\%$, then the northward shift is a permanent feature, or *(ii)* if $p_1 = 54\%$, then the apparent northward shift is a transient feature with lesser connection to the next possible eruption.

The degree of belief in a uniformly distributed background for the prior fault map compared to available tectonic information. The degree of belief in a uniformly distributed background is p_2; the degree of belief in available tectonic data is $1-p_2$. The

random value of p_2 varies inside the interval [0%−50%] assuming that it is unreasonable for the overall available tectonic data to be weighted less than a uniform random distribution representing the lack of information about potentially unmapped faults.

The degree of belief in the pre-14 ka fault extension sub-datasets for the Mono region compared to the most recent dataset. The degree of belief in the pre-14 ka fault extension data is p_3; the degree of belief in the most recent data is $1 - p_3$. The The value of p_3 is randomly sampled inside the interval [0%−100%].

Two alternative models for estimating the distance bound δ, from fault outcrops to the vents potentially related to them. One model uses a 5 km distance depending on the brittle/ductile transition depth, the other uses a 1 km distance depending on numerical models for dike propagation. The degree of belief in the 5 km bound is p_4; the degree of belief in the 1 km bound is $(1-p_4)$. Neither approach is expected to be more reliable without additional information. Hence, p_4 is uniformly sampled inside the interval [0%−100%].

Similar to *Bevilacqua et al.* (2015), different map layers are linearly combined with specific weights, q_j, where $j = 1, \ldots, n$, for the development of a total vent opening map that includes all information (see also, *Chapman et al.*, 2012). While the layers in the earlier work directly correspond to different key features/datasets, here the layers are associated with three different conceptual models, Model 1, Model 2 and Model 3. Following this multi-model approach, each weight represents the probability of the corresponding model to be the correct one in the forecast, assuming that one of the models is correct. Figure 5 illustrates the logic of this vent opening model combination. The linear weights, q_1, q_2, q_3, associated with each of these models, are constrained through a BMA procedure detailed in Appendix A.

Model 1 is an anisotropic Gaussian kernel density estimation based exclusively on the distribution of past vents. In general, a kernel density estimator is a way of smoothing past data (*i.e.,* vent locations) into a probability density that best represents the location of a potential future event that comes from the same underlying population as the observed data. The smoothing is determined by the bandwidth (*e.g., Bebbington & Cronin*, 2011; *Connor et al.*, 2012; *Mazzarini et al.*, 2016). The kernel function describes the expected distance of propagation of new eruptive vents from pre-existing vents. The Bayesian procedure adopted for estimating the bandwidth, as well as the possibility of including a drift, are novel elements in our study.

Model 2 assumes that fault outcrops (*i.e.* mapped faults) provide information for forecasting vent locations (*e.g., Felpeto et al.*, 2007; *Cappello et al.*, 2012, 2015). New vents are expected to more likely occur near mapped faults. We consider only the structures which are more likely to have previously interacted with the rise of magma (see also *Martin et al.*, 2004; *Jaquet et al.*, 2012). Thus, our procedure is based on the update of tectonic data using the likelihood for preferred paths of dike intrusion in the past. The application of a Bayesian procedure on fault data is another novel element in our study.

Model 3 is a uniformly distributed probability map inside a conservative (*i.e.,* large) distance range, basically the maximum recorded distance of past vents from the nearest pre-existing vent after 180 ka. We use a 20 km range from past vent locations, excluding regions above 3000 m if not within a 5 km range from past vents (red dashed line displayed in Figures 7 and 13). Model 3 is included mainly to consider the effect of potentially missing information, complementing the first two models which neglect the presence of unknown vents, and has a remarkably larger spatial extent than the others. Similar uniform probability distributions have been implemented in *Selva et al.* (2012) and *Bevilacqua et al.* (2015) for the same reason.

The 3000 m elevation threshold has been included in Model 3 because LVVR is close to the Sierra Nevada, and there is a very low probability for a non-volcanic peak to become a vent (most of the area is about 2000 m in elevation, so this implies a 1000 m altitude difference). The additional 5 km threshold corresponds approximately to the range of Mammoth Mountain peripheral activity, which is the only place where vent locations were recorded above 3000 m. We also rely on the geological assumption that future volcanism is expected near past activity. Model 1 directly relies on past vent locations, and Model 2 considers mapped faults that are closer to past vent locations. None of the vents after 180 ka opened farther than 20 km from previously active vents, so this assumption is also included in the more conservative Model 3.

However, we conducted a sensitivity analysis on the 20 km threshold. Reducing this threshold to a smaller value slightly increases the average hind-casting performance of Model 3, but assigns zero likelihood to some of the past events. Indeed, 20 km is the maximum range that was observed in our record, and it is also the distance separating the foci of State A

and State B; a shorter threshold distance would not have been able to forecast the jump that occurred at ~60 ka. Hence, assuming a threshold range for the uniform map that is below 20 km is not geologically consistent with past activity. In contrast, increasing the range of the uniform probability map above 20 km significantly reduces the hind-casting performance of the model. Future research aimed at more accurate estimates of the low probability of unexpected large jumps in the volcanic vent pattern could allow for more detailed estimates at the boundary of the domain, but this is beyond the purposes of our study (see also *Bebbington*, 2015).

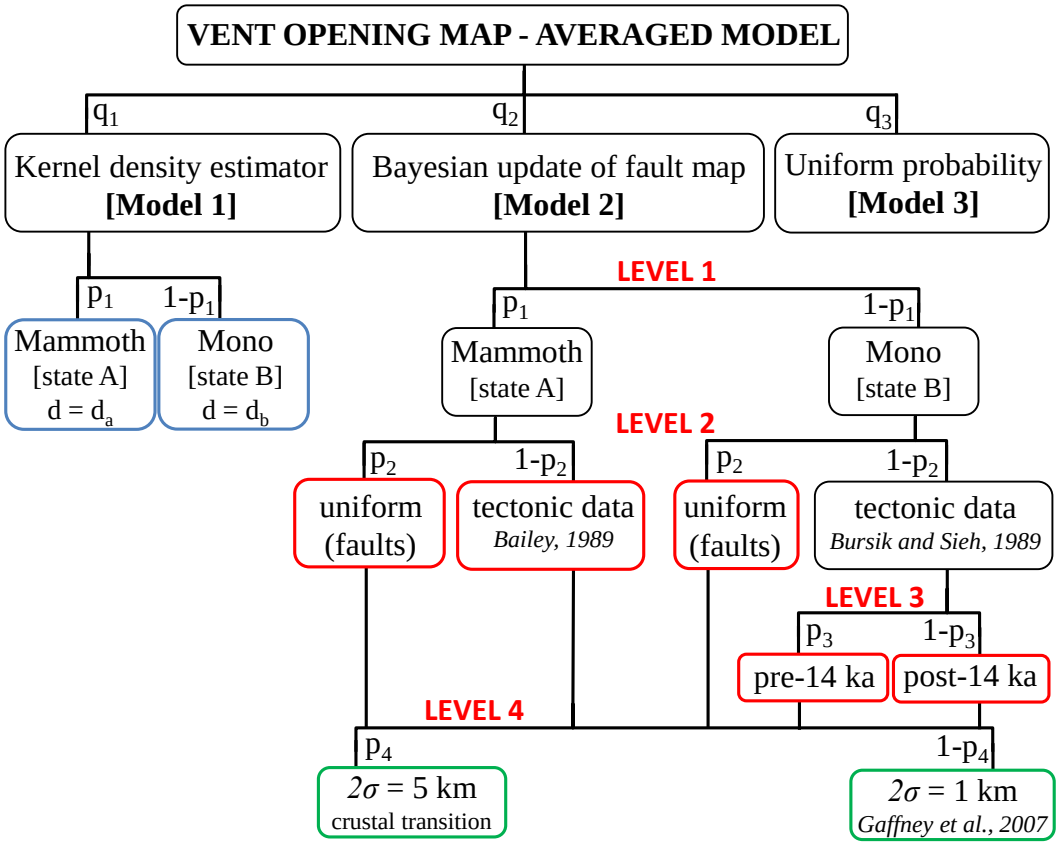

Figure 5: Logic tree of the multi-model scheme, presenting epistemic uncertainty sources. Random variables modeling epistemic uncertainty sources are displayed. Blue boxes show two layers of vent opening map in Model 1. Red boxes show five layers of prior probability of tectonic parameters, and green boxes show two models for likelihood of vent location.

3.1 Kernel density estimation for past vents propagation (Model 1)

Kernel density estimation is a non-parametric method for estimating the spatial density of future volcanic events based on the locations of past vents (*Bebbington & Cronin*, 2011; *Connor et al.*, 2012; *Mazzarini et al.*, 2013; *Bevilacqua et al.*, 2015). The kernel function can be any positive function $\mathbf{K}$ that integrates to one; in this study $\mathbf{K}$ is assumed to be a two-dimensional anisotropic Gaussian density. A Gaussian density is completely described by its mean (or drift), μ, and the covariance (or bandwidth) matrix, $\mathbf{\Sigma}$.

Given the locations (x_i, y_i), where $i = 1, \ldots, N$ of N past events, we allow a new event to propagate some random distance from a given location, which is sampled from the kernel function. That is,

$$\mathbf{X} = (x_k + d_1, y_k + d_2)\,, \tag{1}$$

where $\mathbf{X}$ is the spatial location of the next vent, k is a discrete random variable in a $1, \ldots, N$ sampling of one of the previous vents, and $\mathbf{d} = (d_1, d_2)$ is a two dimensional Gaussian random vector with mean μ and covariance matrix $\mathbf{\Sigma}$. A small complication in our study is that the past vent locations do not comprise points, but instead disks of uncertainty, and each vent area partially covers more than one cell of our grid. Therefore for each cell we take into account the fraction of each vent disk that it contains and then we apply the kernel convolution to this value. It is significant that the adoption of anisotropic kernel functions allows for directional features, which are particularly relevant in the Mono region.

Following this method, the only source of uncertainty affecting the results arises from the possibility of eruptions jumping between the Mammoth Mountain region (State A) and the Mono region (State B). The uncertainty sources previously listed concern the tectonic information. The random variables k and d change with the state; we define them as k_A, d_A for State A and k_B, d_B for State B. Without additional information being available, the variables $(k_j), j = A, B$, are assumed to be equally distributed on the $(N_j), j = A, B$, vents belonging to the considered state, and in particular:

$$P[k_A = i] = \frac{1}{N_A}, \forall\, i \leq N_A$$
$$P[k_B = i] = \frac{1}{N_B}, \forall\, i \leq N_B$$

The estimation of the variables (d_j), where $j = A, B$, relies on the statistics of the distances of propagation observed in the past. They are characterized by their mean values μ_A and μ_B, and their covariance matrices $\mathbf{\Sigma}_A$ and $\mathbf{\Sigma}_B$.

The complete kernel can be expressed as follows. For each $j = A, B$, the density f_j of $\mathbf{X}$ conditioned on being in the State j is the convolution of the kernel function describing d_j with the past vent location disks $(D_i), i = 1, \ldots, N_j$, each weighted by the distribution of k_j:

$$f_j(x) = \sum_{i=1}^{N_j} \frac{1}{2N_j\pi\sqrt{det(\Sigma_j)}} \int_{D_i} exp\left(-\frac{1}{2}\left(\mathbf{x} - \xi - \mu_j\right)^T \Sigma_j^{-1} \left(\mathbf{x} - \xi - \mu_j\right)\right) d\xi. \tag{2}$$

The combined formula adopted for defining the final density is

$$f = p_1 f_A + (1 - p_1) f_B. \tag{3}$$

Mean values $(\mu_j), j = A, B$, and covariance matrices $(\mathbf{\Sigma_j}), j = A, B$, for State A, are obtained from propagation distances of the 35 most recent vents in State A. The 9 oldest vent locations (Subset 1 defined above) serve as an initial distribution, necessary for the definition of the propagation distances. For State B we consider the 30 most recent propagation distances (Subset 4), using the 7 older State B vents as an initial distribution. This estimate also depends on the pre-existing vent from which we are measuring. We consider measuring from the spatially closest vent, or from the second closest vent (and of course one could continue looking farther afield), and find very different results.

Alternative estimates are produced considering all the different distances from the n^{th} closest pre-existing vent for $n = 1, \ldots, 7$. They produce different drifts, different bandwidth matrices, and hence different shapes for the propagation kernels. The combination of these distance measurements is done following a Bayesian Model Averaging (BMA) procedure based on a hind-casting validation of the most recent part of the State A and State B datasets (25 events); this procedure is detailed in Appendix A.

Our procedure is different from the bandwidth selection methods based on least-squares cross-validation (LSCV) (*Duong*, 2007), or on the sum of asymptotic mean squared error (SAMSE) (*Duong & Hazelton*, 2003). The LSCV and SAMSE methods both rely on the mean integrated squared error (MISE) criterion,

$$MISE(f) = E\left[\int_{\mathbb{R}^2} |f(x) - g(x)|^2\, dx\right], \tag{4}$$

to measure the performance of the estimated density f compared to the target density, g, (*i.e.,* the unknown density from which the data points are sampled). MISE depends on g, and the methods cope with this through plug-in estimates (SAMSE) and cross-validation techniques (LSCV). Model 1 of this study does not make a comparison with any target

density, g, but instead focuses on the distances between new data points (*i.e.,* vents) and the pre-existing data points (see also *Magill et al.*, 2005). We use the temporal sequence of data, and this also enables us to compute a drift in the propagation pattern, together with the covariance matrix.

Other bandwidth selection methods are based on the maximization of the Kullback-Leibler score, S, inside a cross-validation procedure (*Vere-Jones*, 1992; *Bebbington*, 2015). In particular:

$$S = \sum_{i \in \Theta} log f(x_i) - \int_{\mathbb{R}^2} f(x) dx, \tag{5}$$

where $(x_i), i \in \Theta$, are the data point locations selected for the validation, and f is computed using the other data points. In our vent opening mapping problem (spatial estimates only, not including time), the second term of this sum is equal to one, and maximizing S is equivalent to maximizing the log-likelihood of the data points inside Θ. Model 1 of this study is different because it relies on the temporal sequence for setting up the validation procedure instead of following a cross-validation approach. Moreover we implement BMA on a set of possible bandwidth models instead of relying on a single maximum likelihood estimator. Significantly, all of our prior bandwidth models use only nearest data point (pre-existing vent) information, hence the corresponding estimator can be inconsistent and the BMA at least partially compensates for this.

Because of its similarity to our approach, we make a comparison of Model 1 with the spatio-temporal nearest-neighbor estimate approach detailed in *Connor & Hill* (1995), concerning the production of vent opening maps in the Yucca Mountain region (Nevada). Similarly, their method also uses information from only the nearest vents. The procedure includes temporal information, weighting vents inversely according to $\Delta t \Delta x^2$. In our approach, the reduced weight of State A follows a similar reasoning. However, the LVVR temporal record ranges over almost three orders of magnitude, and the relevance of State A activity in the spatio-temporal nearest-neighbor analysis is significantly smaller than in our approach. In contrast, a spatial nearest-neighbor analysis gives a larger relevance to the State A activity, because of the strong spatial clustering of past vents in that region.

3.2 Bayesian update of fault extension maps (Model 2)

Model 2 merges tectonic data and past vents locations following a Bayesian approach. The vent opening map depends on an additional spatial parameter $\zeta = (\zeta_1, \zeta_2)$ representing the outcrop of the fault interacting with a future potential rising dike. First, we obtain the prior distribution of ζ from the available fault extension dataset. Next, we calculate the posterior distribution of ζ given the observation of past vent locations and a Gaussian likelihood function concerning the expected distance of faults and vents. Finally, we convolve the likelihood function with the posterior distribution of ζ for calculating the vent opening probability map.

This is a different approach from the one reported in *Martin et al.* (2004). In that study, various strands of geophysical data were implemented as likelihood functions to update the prior vent opening probability distribution based on the spatio-temporal pattern of past events. In our study, the roles of parameter and observation are the inverse of those.

In the following, we detail the construction of the prior probability distribution of ζ including the sources of uncertainty previously described. The prior probability is assumed to be uniformly distributed on a 100 m buffer along fault scarps, weighted in proportion to their extension rate measurements in a log-scale of 10 μm per year units. State A and State B of the system correspond to separate prior probability maps, respectively based on *Bailey* (1989) and *Bursik & Sieh* (1989) datasets. In particular, we define two alternative maps for State B, assuming the pre-14 ka maximal extension rates or the post-14 ka extension rates. We also include an additional uniformly distributed probability map for considering the incompleteness of this tectonic information. This uniform probability distribution has a different meaning than the one in Model 3. These maps are not vent opening maps, but rather probability maps of the tectonic parameter ζ. In total, we consider four alternative prior probability maps, each of them associated to a different degree of belief (m_i), $i = 1, \ldots, 4$, influenced by the epistemic uncertainty parameters (p_i), $i = 1, 2, 3$.

These degrees of belief are:

$m_1 = (1 - p_1)(1 - p_2)p_3$, for State B pre-14 ka tectonic data,

$m_2 = (1-p_1)(1-p_2)(1-p_3)$, for State B post-14 ka tectonic data,

$m_3 = p_1(1-p_2)$, for State A tectonic data,

$m_4 = p_2$, for a uniform probability distribution.

The sum of these four degrees of belief is equal to one, and a simple logic tree (presented in Figure 5) underlies their definition from the parameters $(p_i), i = 1, 2, 3$.

Conditioned on the tectonic parameter value $\zeta = (\zeta_1, \zeta_2)$, we define the likelihood for a vent location $\mathbf{x}$ as a symmetrical, two dimensional Gaussian function of mean ζ and covariance matrix $\sigma^2\mathbf{I}$:

$$g(\mathbf{x}|\zeta) = \frac{1}{2\pi\sigma^2} exp\left(-\frac{1}{2\sigma^2}\|\mathbf{x}-\zeta\|^2\right) \tag{6}$$

The value of the standard deviation, σ, is related to the distance bound from the fault outcrops to the vent openings related to them: 5 km, depending on the brittle/ductile transition depth, or 1 km, depending on the numerical models for dike propagation. In particular, we assume this bound equal to 2σ, which is the 95^{th} percentile of the one-dimensional projection of the Gaussian likelihood $g(\cdot|\zeta)$ on the unknown dipping direction of the considered fault. The degrees of belief in the two models are p_4 and $(1-p_4)$, respectively.

Then, for each specific past vent location (x_i, y_i), we use Bayes theorem to calculate the posterior probability density values $z(\zeta_1, \zeta_2|x_i, y_i)$ of ζ as the product of the prior density values $z(\zeta_1, \zeta_2)$ and the likelihood $g(x_i, y_i|\zeta_1, \zeta_2)$ values, up to a multiplicative normalization constant C. We integrate past vent locations on their uncertainty disk $(D_i), i = 1, \ldots, N$, according to the expression:

$$z(\mathbf{x}|D_i) = C \cdot \int_{D_i} z(\mathbf{x}) g(\xi|\mathbf{x}) d\xi. \tag{7}$$

A sequential update of several past vent locations would produce an *averaged* dike preferential path. Considering, instead, an ensemble of alternative magma paths for the different events, we calculate different posterior probabilities, one for each of the past vents considered, and we define the global posterior of ζ as the average of them, with equal weights.

This procedure is repeated for the four different prior maps considered for ζ, producing four posterior maps. We define a combined posterior probability map comprehensive of all the possible prior choices by another linear averaging step, weighting the posterior maps for ζ in proportion to the degrees of belief $(m_i), i = 1, \ldots, 4$ listed above. Linear averaging is not commutative with the Bayes theorem; a different result would be obtained by averaging the four prior probability maps instead. We choose to average the posterior probability maps because, by this method, the linear weights directly impact the final results, and they are not altered by the multiplicative step.

Finally, we calculate the vent opening map applying the kernel function $g(\cdot|\zeta)$ to the final posterior probability distribution. In summary, the vent opening probability density g according to Model 2 is defined by:

$$g(\mathbf{x}) = \int_{\mathbb{R}^2} g(\mathbf{x}|\zeta) \sum_{j=1}^{4} \frac{m_j}{N} \sum_{i=1}^{N} z_j(\zeta|D_i) d\zeta, \tag{8}$$

where $(z_j), j = 1, \ldots, 4$ are the prior probability density functions of ζ, $(m_i), i = 1, \ldots, 4$ are their degrees of belief, and $(D_i), i = 1, \ldots, N$ are the uncertainty disks of past vents.

3.3 Stochastic combination of the three models

We have described three conceptual models: *(i)* the kernel density estimation model, *(ii)* the model based on the Bayesian update of the fault map, and *(iii)* the uniform probability model. The purpose of the study is to produce a vent opening map integrating all of the available information, and hence, we will accomplish a linear combination (probability mixture) of the three maps. Because the models are doubly stochastic, this combination will be repeated for each of the sample maps inside a Monte Carlo simulation. Figure 5 illustrates the logic of this vent opening model combination.

The linear weights $(q_i), i = 1, 2, 3$, are a key parameter in this approach. In *Bevilacqua et al.* (2015) expert judgment techniques were adopted to constrain the linear weights; in contrast here, we will follow a Bayesian model averaging approach, relying on how the three models performed to hind-cast the 25 most recently active vent locations based on the older data. The weights $(q_i), i = 1, 2, 3$ coincide with the model scores $s(i), i = 1, 2, 3$ (see Appendix A).

4 Results and discussion

First, we separately describe each model's detailed results, then we present the linear weights and the combined maps.

4.1 Kernel density estimator map (Model 1)

The key elements of Model 1 are the parameters of the kernel function, the mean vector μ and the covariance matrix $\mathbf{\Sigma}$, which depend on the choice of nearby vents used to calculate the vent propagation distance. For example, assuming we measure the distance from the nearest previously active vent (in km), the covariance matrix $\mathbf{\Sigma}_A$ calculated through the unbiased estimator, and the associated (column-wise) eigenvectors (v_1^A, v_2^A) are:

$$\Sigma_A = \begin{bmatrix} 1.218 & 0.240 \\ 0.240 & 0.974 \end{bmatrix} \qquad (v_1^A, v_2^A) = \begin{bmatrix} -0.852 & 0.523 \\ -0.523 & -0.852 \end{bmatrix} \tag{9}$$

In State A, both the covariance matrix and the eigenvectors do not show a large anisotropy. This distance is the most likely according to the BMA procedure (Table 1). Concerning State B, the more likely results are, instead, obtained considering the distance of each vent in the sequence from the 3^{rd} closest pre-existing vent (Table 1). The covariance matrix $\mathbf{\Sigma}_B$ and the eigenvectors (v_1^B, v_2^B) are in this case:

$$\Sigma_B = \begin{bmatrix} 1.637 & -1.183 \\ -1.183 & 16.656 \end{bmatrix} \qquad (v_1^B, v_2^B) = \begin{bmatrix} -0.078 & -0.997 \\ 0.997 & -0.078 \end{bmatrix} \tag{10}$$

In State B, the covariance $\mathbf{\Sigma}_{B,22}$, concerning the N−S direction, is an order of magnitude larger than $\mathbf{\Sigma}_{B,11}$. The first eigenvector is directed north, compatible with the strike direction of the main faults.

For both the State A and State B calculations, the mean vector μ, which represents a mean drift in the propagation distance, is less than 300 m and does not significantly affect the results.

Table 1: The BMA weights, bandwidth selection for Model 1.

Scores	$\mathbf{M}_1$	$\mathbf{M}_2$	$\mathbf{M}_3$	M_4	M_5	M_6	M_7
State A (s^A)	99.70%	0.19%	0.06%	0.05%	0.00%	0.00%	0.00%
State B (s^B)	0.00%	0.53%	71.13%	23.82%	0.48%	3.89%	0.14%

Considering the i^{th} spatially closest pre-existing vent for $i = 1, \ldots, 7$, different estimates are produced. We linearly averaged the alternative kernel density functions accordingly to the BMA scores presented in Table 1 (also described in Appendix A).

Figure 6 shows an example of the effect of BMA on the kernel functions. On the left are the plots of the average kernel function adopting prior scores, while on the right are the results with posterior ones. The reduction of variance is due to the fact that higher index models do not get large scores.

The vent opening maps presented in Figure 7 are the estimates for the probability of vent opening per km^2 in each point in the region of interest according to the described model. The maps have their own confidence intervals due to the effects

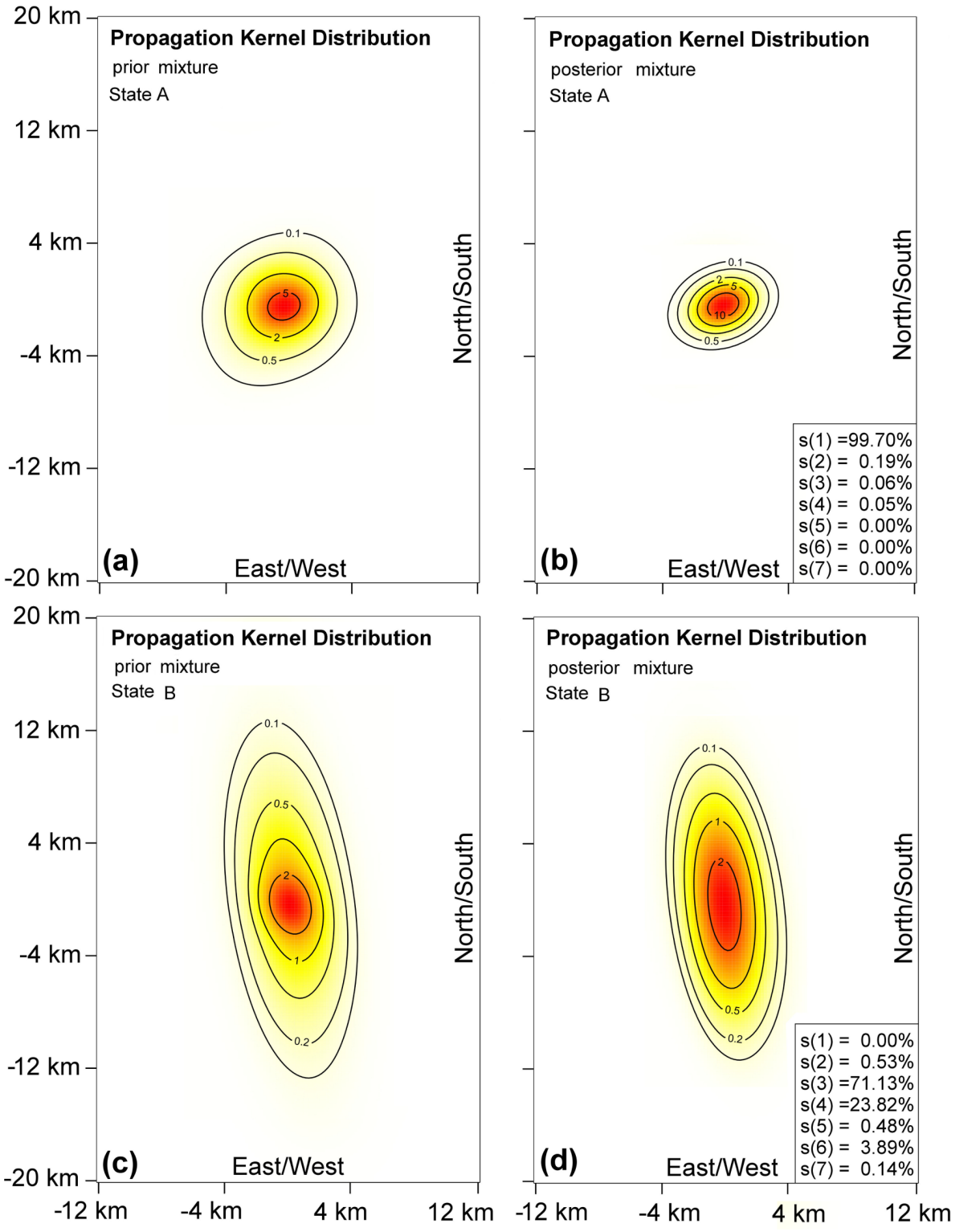

Figure 6: Plots of kernel distributions. Colors and numbers show probability as a percentage per km^2. Frames (**a** and **c**) show mixtures assuming equal weights $s(i), i = 1, \ldots, 7$. Frames (**b** and **d**) present the posterior weights.

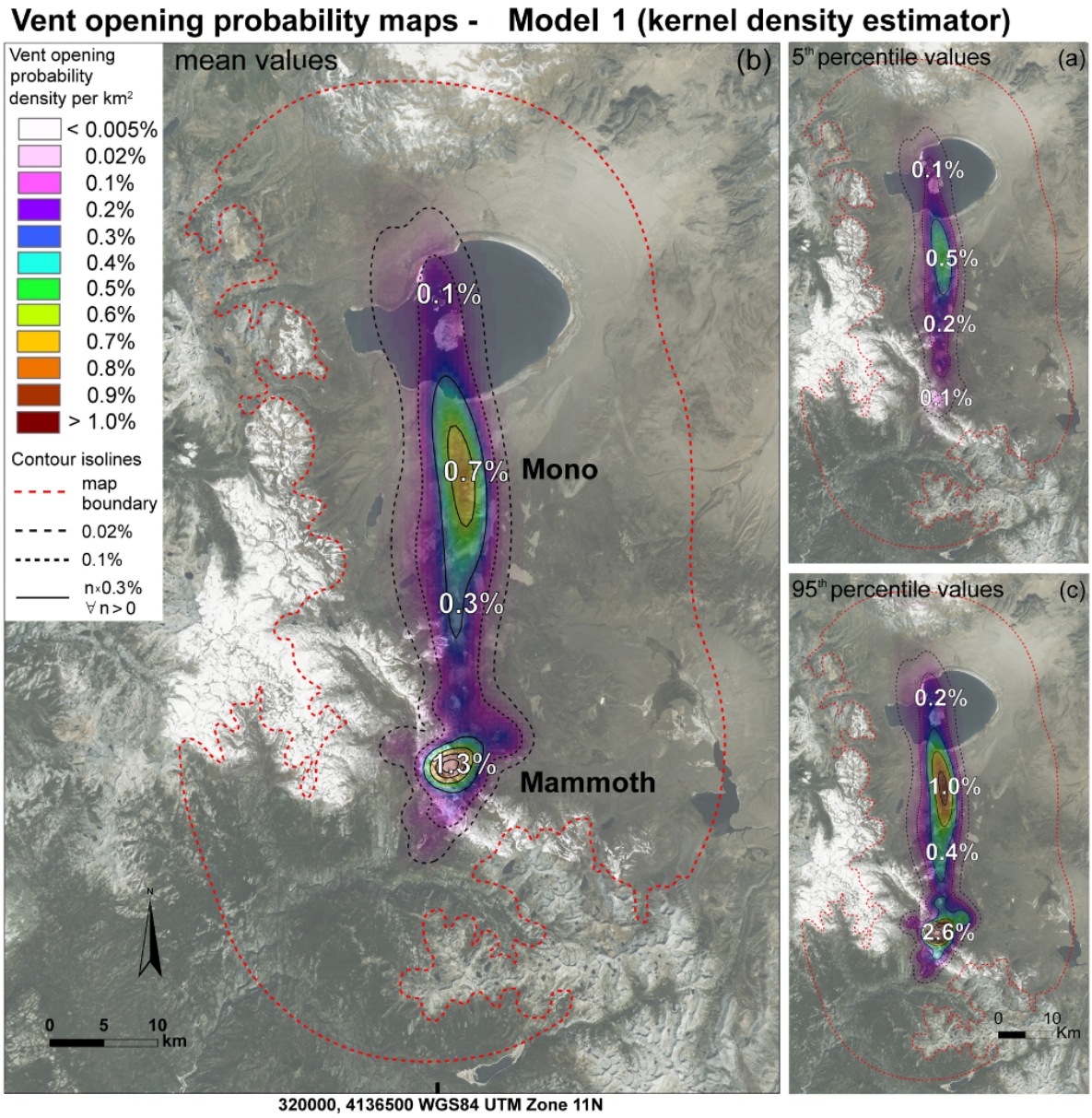

Figure 7: Spatial vent opening probability maps for LVVR based on kernel density estimation method. In (**a**) we show the 5^{th} percentile values, in (**b**) the mean values, and in (**c**) the 95^{th} percentile values of the probability. Color, contours and numbers show probability as a percentage per km^2. Black lines are 0.3% spaced, dashed lines mark 0.1% and 0.02% probability density levels. Red dashed line marks the map boundary (described in Model 3).

of epistemic uncertainty on parameter p_1, *i.e.,* the unknown relevance of Mammoth Mountain (State A). For this reason three maps are displayed, showing the 5^{th} percentile, the mean and the 95^{th} percentile values.

Colors and contour lines show the vent opening probability as a percentage per km^2. The thin red dashed line marks the current domain boundary, a 20 km range from past vents locations, excluding places above 3000 m if not in a 5 km range from past vents. The local maxima of the probability are clearly localized around Mammoth Mountain in the south and the Mono-Inyo Craters range in the north. The mean probability density values per km^2 are about 1.3% and 0.7% respectively, indicating a more peaked probability in the Mammoth Mountain region. However, this does not produce a remarkably higher integral of probability because the Mono region covers more than twice the area width, specifically detailed for the combined maps. The relevant epistemic uncertainty about the real relevance of State A activity, compared to that of the younger State B, has the effect of making the 5^{th} percentile maxima of densities in the two sub-regions 0.1% and 0.5% respectively, whereas the 95^{th} percentiles are instead 2.6% and 1.0%, respectively.

4.2 Bayesian update of the fault map (Model 2)

The posterior probability distribution of ζ is presented in Figure 8, with specific colors indicating the probability density value per km^2 of this tectonic parameter. A black line bounds the 0.02% probability density per km^2. Areas of high probability closely follow the fault outcrops which are proximal to past activity. However, the largest random p_2 values, associated with the uniformly distributed probability map, produce a higher probability further from the mapped faults.

Figure 9 shows the vent opening maps obtained from Model 2, according to the previously described tectonic data. The maps have their own confidence intervals due to the effects of epistemic uncertainty on parameters $(p_i), i = \ldots, 4$, and again three maps are displayed, showing the 5^{th} percentile, the mean and the 95^{th} percentile values. The mean map shows what we obtain if we average the different conceptual models according to their degrees of belief $(m_i), i = 1, \ldots, 4$, and the percentile maps display what may change according to the uncertainty that affects such degrees of belief.

In this case, the maximal mean values at Mammoth Mountain and around Mono craters are 1.7% and 2.1% per km^2, indicating that the distribution is more peaked than following Model 1, reducing the difference between the north and south sub-regions. The south maximum drops to 0.1% in the 5^{th} percentile map, while the north is 0.5%. The 95^{th} percentile maxima reach 4.5% and 4.1%, respectively. A secondary maximum is also present in the Mono Lake zone, reaching a mean of 1.0%. Because of epistemic uncertainty affecting the estimates about the distance from fault outcrops and new vents (5 km or 1 km), the 95^{th} percentile map shows more widely spread high density values, while the 5^{th} percentile map is more narrowly following the main fault lines.

4.3 Combined vent opening probability maps

Table 2: The BMA weights for multiple models.

Scores	**5^{th} percentile**	**mean**	**95^{th} percentile**
Model 1 (q_1)	33.06%	**38.73%**	46.76%
Model 2 (q_2)	41.19%	**51.90%**	57.22%
Model 3 (q_3)	07.62%	**09.38%**	11.30%

Using the BMA procedure described in Appendix A, we obtain the weights $(q_j), j = 1, 2, 3$, adopted for a linear combination of the three alternative conceptual models developed: *(i)* the kernel based method (Model 1), *(ii)* the Bayesian update of tectonic data (Model 2), and *(iii)* the uniformly distributed probability map (Model 3). These estimates are affected by epistemic uncertainty depending on the uncertain parameters $(p_i), i = 1, \ldots, 4$. Hence, the distributions of $(q_j), j = 1, 2, 3$ are described by their mean values, 5^{th} percentiles and 95^{th} percentiles and calculated using the BMA algorithm in a Monte Carlo simulation which randomly sampled the value of the $(p_i), i = 1, \ldots, 4$; these are presented in Table 2. Model 2

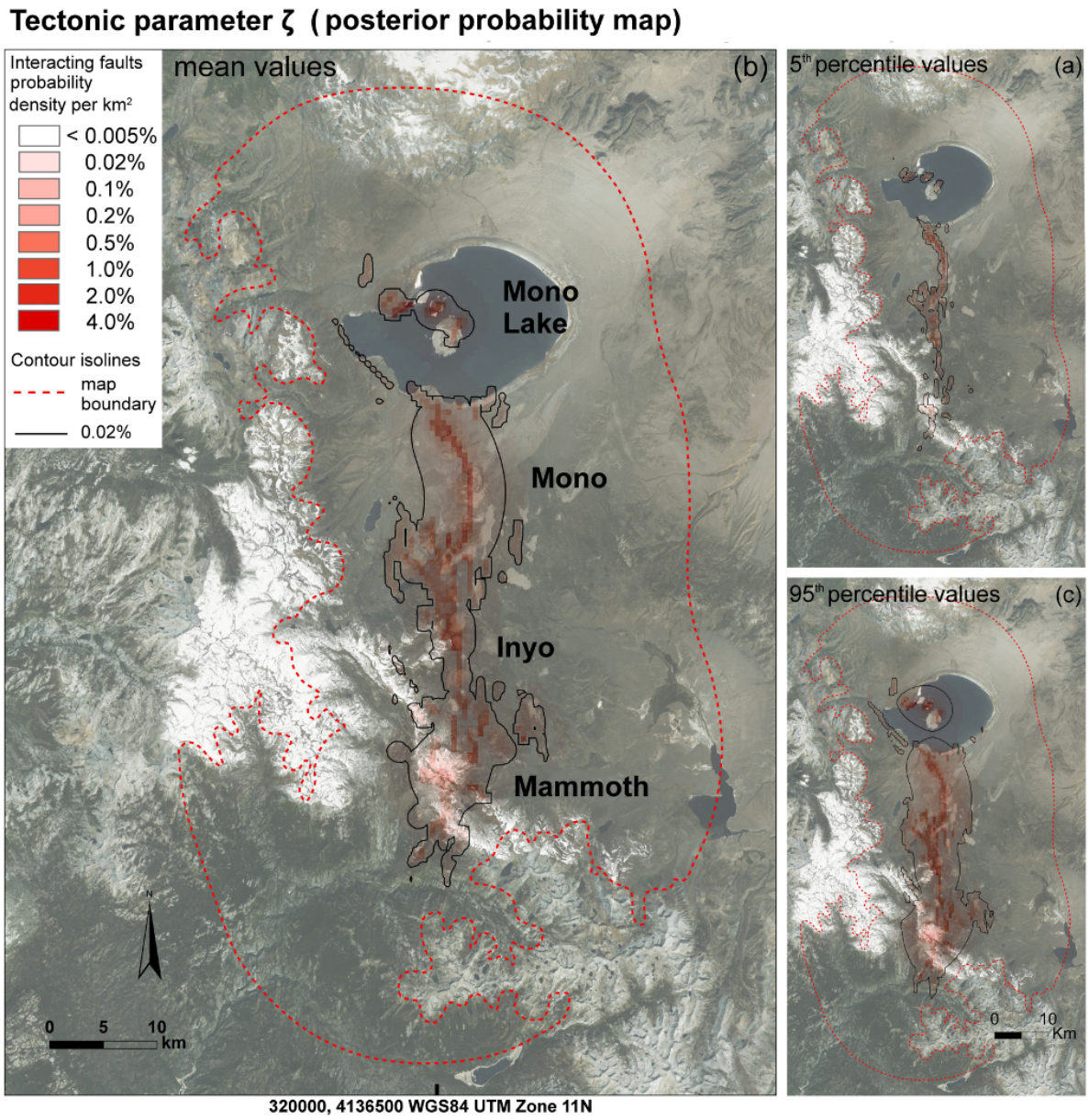

Figure 8: Tectonic parameter ζ posterior probability distribution, after past vents data. (**a**) shows the 5^{th} percentile values, (**b**) the mean values, and (**c**) the 95^{th} percentile values of the probability. Color and contours show probability as a percentage per km^2. Black lines mark the 0.02% probability density level. Red dashed line marks the map boundary (described in Model 3).

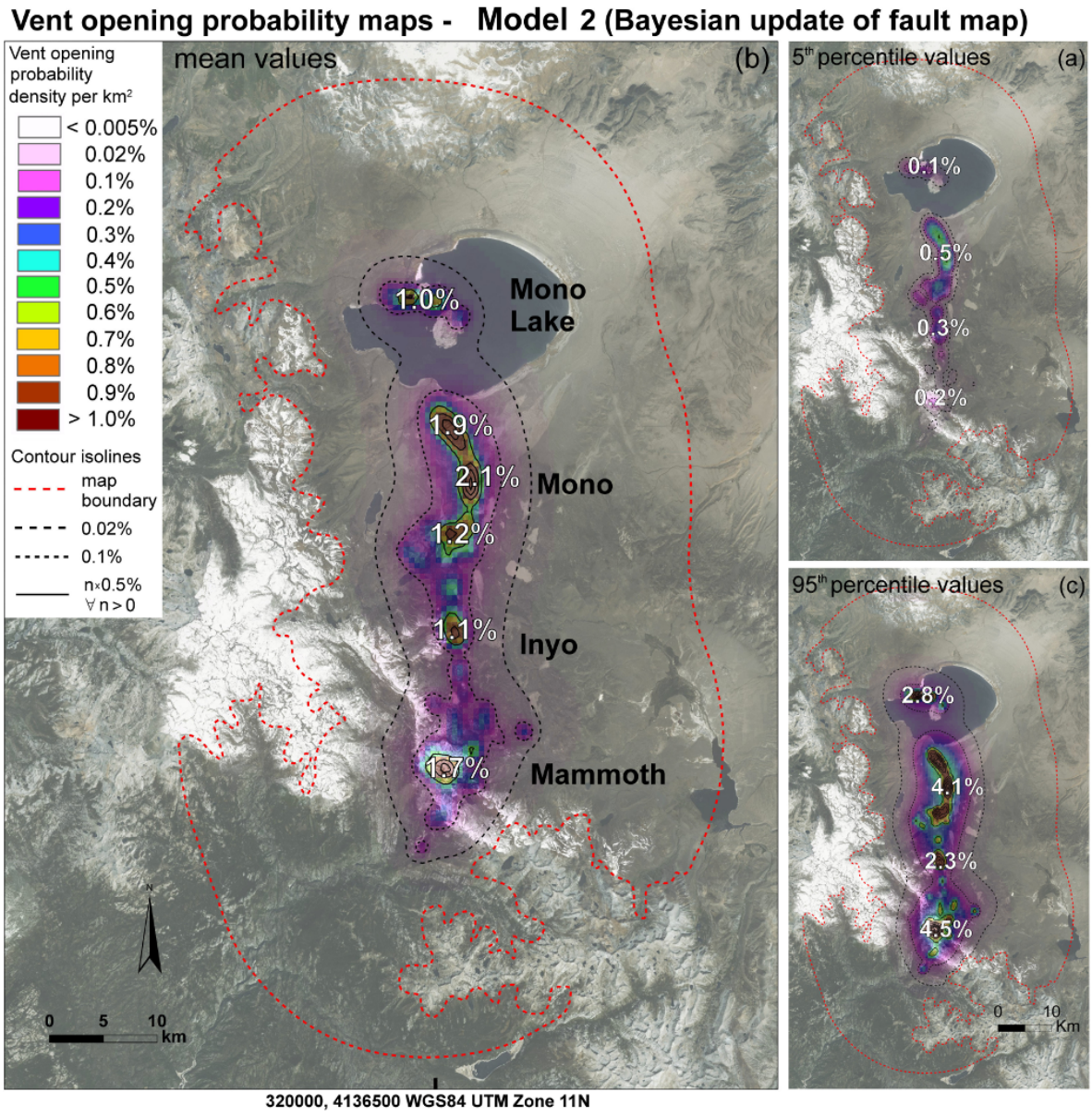

Figure 9: Spatial vent opening probability maps for LVVR based on Bayesian update of tectonic data. In (**a**) we show the 5^{th} percentile values, in (**b**) the mean values, and in (**c**) the 95^{th} percentile values of the probability. Color, contours and numbers show probability as a percentage per km^2. Black lines are 0.5% spaced, dashed lines mark 0.1% and 0.02% probability density levels. Red dashed line marks the map boundary (described in Model 3).

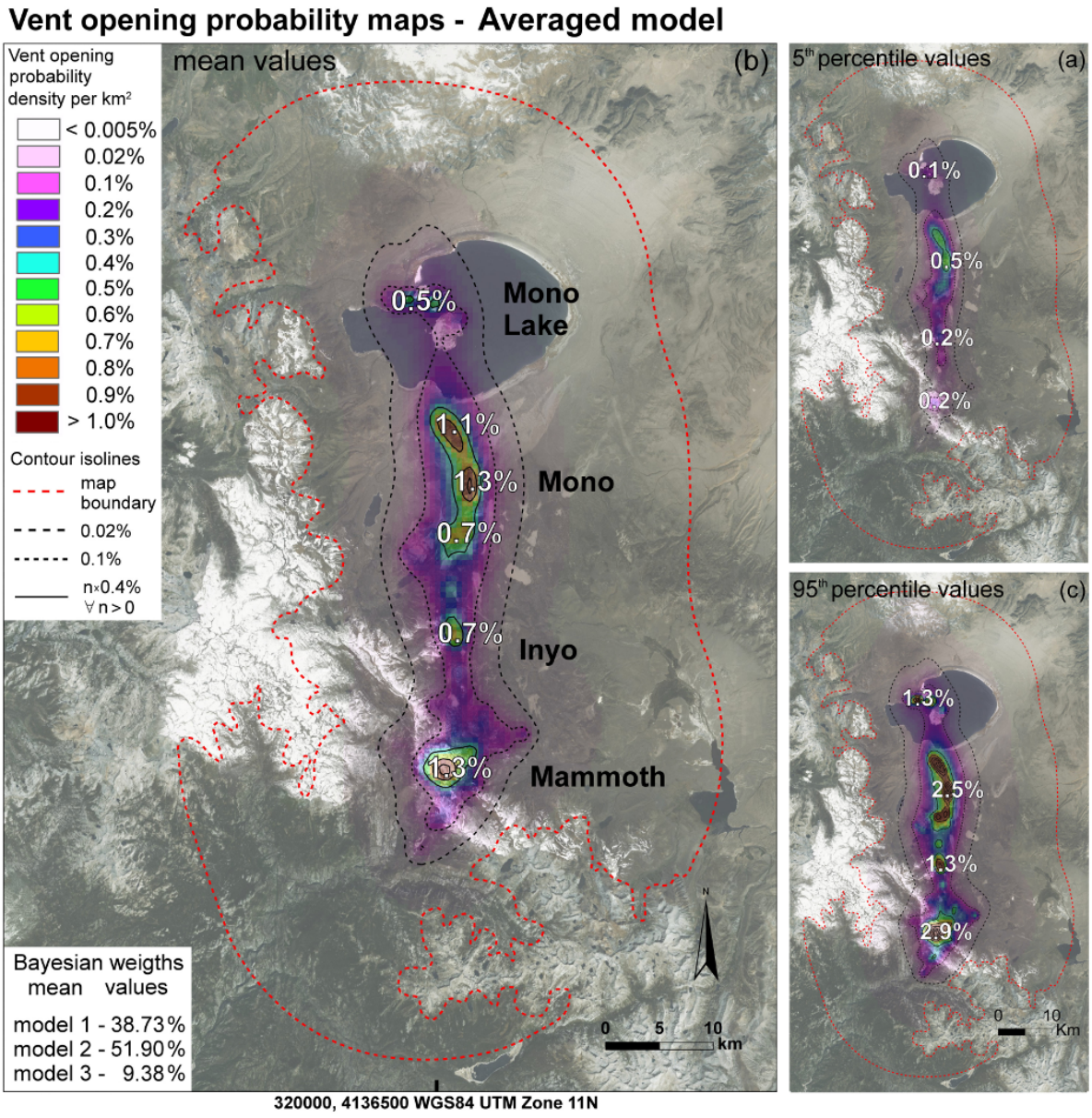

Figure 10: Spatial vent opening probability maps for LVVR based on three averaged models (BMA). In (**a**) we show the 5^{th} percentile values, in (**b**) the mean values, and in (**c**) the 95^{th} percentile values of the probability. Color, contours and numbers describe probability as a percentage per km^2. Black lines are 0.4% spaced, dashed lines mark 0.1% and 0.02% probability density levels. Red dashed line marks the map boundary (described in Model 3).

weights at more than half of the total probability, but Model 1 is still significantly relevant, gaining more than one third of the total probability.

It is helpful to compare these results with those of *Bevilacqua et al.* (2015). Here the uncertainty bounds are significantly narrower, and the uniformly distributed probability map received a smaller weight, compared with the *Bevilacqua et al.* (2015) findings. These differences arise not only from the different features of the two volcanic systems studied, but also from the different statistical approaches followed, an expert judgment analysis in the former study and BMA in this study.

Figure 10 shows the averaged model map using the BMA weighted combination. Again, maps of the 5^{th} percentile, the mean and the 95^{th} percentile values are shown. The average maxima of 1.3% probability per km^2 in the Mammoth and Mono regions are equal, but such probability values in the north region cover a much larger extension. The Mono Lake secondary maximum reaches a mean of 0.5% per km^2. The Mammoth and Mono region maxima reach 2.9% and 2.5%, respectively, in the 95^{th} percentile maps, but are reduced to 0.2% and 0.5% in the 5^{th} percentile map. The uniform probability distribution produces a probability minimum of at least 0.0032% per km^2 inside the red dashed boundary displayed in the figure.

We also estimate the complementary probabilities of a new event opening in the northern and in the southern parts of LVVR, according to a separation line at the northernmost point of LVC boundary (4180952 northing, WGS84 UTM Zone 11N and marked as a black dot in Figure 11. They are described as average probability values and 5^{th} percentiles and 95^{th} percentiles due to epistemic uncertainty effects: North [45.87%, 63.56%, 84.70%], South [15.30%, 36.44%, 54.13%]. Additional estimates are possible for any specific subset of the region.

Figure 11 shows the density function of the marginal South-to-North direction of the vent opening probability, *i.e.,* the integral of the bivariate probability distributions shown in Figures 7, 9 and 10, along the horizontal (E−W) direction. This enables us to plot a one-dimensional summary of the vent opening maps. In Figure 11**a** we show the mean and percentile curves obtained from the kernel density estimator method, in Figure 11**b**, the percentile curves from the Bayesian update of the fault map, and in Figure 11**c**, the averaged model results. Figure 11**d** shows a comparison between the mean density functions of the different models. For the sake of completeness we also include the marginal density of the uniform probability distribution (Model 3), which is not constant because of the varying width of the area.

In Figure 11 (**a**, **b** and **c**), the parts of the curve corresponding to Mammoth Mountain and Mono Craters are labeled. The higher level of uncertainty affecting the former is characterized by the larger spread between the percentile lines. In Figure 11 (**b** and **c**), the parts corresponding to Inyo craters and Mono Lake are labeled, characterized by local maxima in Model 2. The averaged model produces curves intermediate to those of Models 1 and 2, with a smaller effect from Model 3, reducing the spikes in the 95^{th} percentile curve and producing a low probability *tail* at the boundary of the volcanic region.

Conclusions

We have developed a new spatial map of the long-term probability of vent opening, conditioned on the occurrence of a volcanic eruption in the LVVR region. The estimates are based on the most up-to-date information of the distribution of past eruptive vents after 180 ka, from literature (*Bursik & Sieh*, 2013; *Hildreth & Fierstein*, 2016) and new field work, and from fault locations and their extension rates (*Bailey*, 1989; *Bursik & Sieh*, 1989). The doubly stochastic features and BMA approach implemented on logic tree schemes permit the combination of different conceptual models and the production of averaged estimates, including uncertainty quantification. Our map represents crucial input information for the development of quantitative long-term hazard zonation of potential hazardous eruptive phenomena in the LVVR, such as pyroclastic density currents and tephra fallout (*Miller et al.*, 1982; *Bayarri et al.*, 2009, 2015; *Neri et al.*, 2015; *Volentik & Houghton*, 2015; *Sandri et al.*, 2016). The vent opening map may also be used as the basis for generating updated short-term probability assessments, once monitoring information is integrated. Additional research aimed at a more detailed modeling of the temporal record in the LVVR region would be relevant, and a specific uncertainty quantification concerning temporal completeness of the record is fundamental to improve the current analysis. Our most significant results include the following:

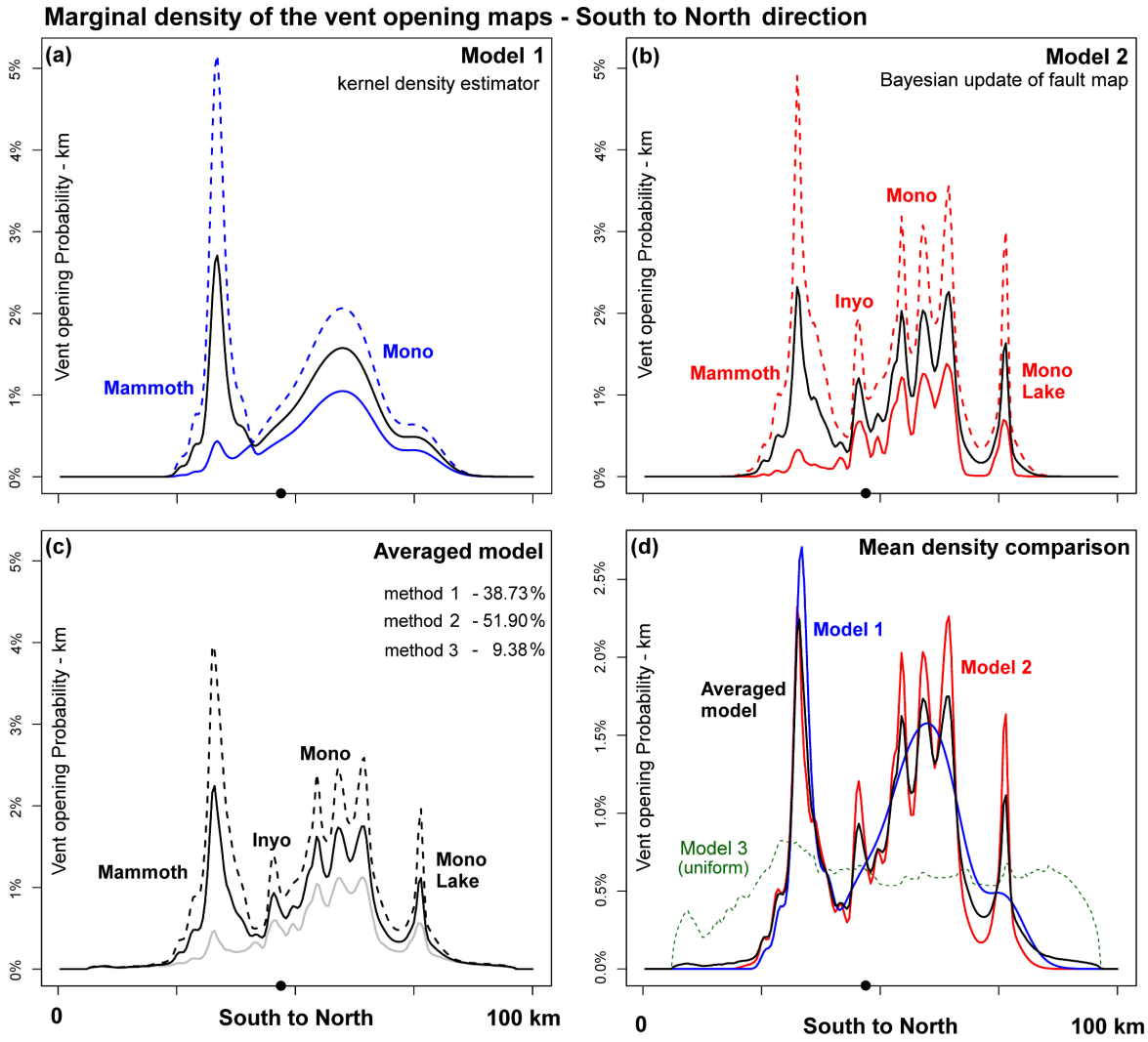

Figure 11: Marginal density functions of the vent opening probability maps for LVVR, along the South-to-North direction. Shown are (a) Model 1, (b) Model 2, (c) the averaged model results. Black curves describe the average values, continuous colored curves the 5^{th} percentile values, dashed colored curves the 95^{th} percentile values of the probability density per km. (d) shows a comparison of the mean density functions, different colors describe the different models. A black dot marks the northernmost point of LVC boundary.

1. Through the application of a doubly stochastic model, our map explicitly accounts for the presence of relevant sources of epistemic uncertainty in relation to the interpretation of the LVVR volcanic system. We consider the potential relevance of Mammoth Mountain activity, the time window/completeness of tectonic data, and the range from fault outcrops in which the vent opening probability is increased. In addition to a mean vent opening map representative of the physical variability of the process, we quantify the effects of these epistemic uncertainty sources, and display the 5^{th} percentile and 95^{th} percentile uncertainty bounds at each location.
2. We present a kernel density estimation model with anisotropic properties due to the specific past vents migration pattern relying on a new Bayesian procedure to estimate covariance and drift (Model 1). We present a new Bayesian approach based on tectonic data and observations of past vents locations (Model 2).
3. Three different statistical models are combined through a BMA procedure based on a comparative validation via the hind-casting of the most recent vent locations. This proves to be a versatile tool for comparing and combining different models. We expect that the integration of BMA with expert judgment could improve uncertainty quantification in multi-model frameworks, improving comprehension of target questions, and reducing response bias.

Our results show evidence for two principal high probability sub-regions, one along Mono-Inyo Craters and the other around Mammoth Mountain. The probability density values at the Mammoth Mountain and Mono-Inyo Craters maxima are very similar, but the Mammoth Mountain high-probability sub-region is spatially more localized, and it is also significantly affected by epistemic uncertainty. We calculate the vent opening probability integrals on the north and south parts of the region, obtaining ~64% and ~36% probabilities respectively, with an uncertainty of about ±20%. This is significant to our thinking about the LVVR hazard, as previously the estimation of the hazard related to Mammoth Mountain has tended to be near zero, owing to the age of the edifice as a whole. This result, taken together with the recent mapping and dating by *Hildreth et al.* (2014) and *Hildreth & Fierstein* (2016) of Mammoth Mountain and its periphery suggests that the hazard associated with volcanism in this area should be more fully evaluated.

Acknowledgments

Other data sets and derived data can be requested from the corresponding author (A.B.). The satellite/aerial photos on the background of several figures are from the ESRI dataset *World Imagery* (https://services.arcgisonline.com/ArcGIS/rest/services/World_Imagery/MapServer). This work has been developed during the project Hazard SEES *Persistent volcanic crises resilience in the face of prolonged and uncertain risk*, funded by the National Science Foundation (USA). The contribution and support from many colleagues participating in the above project are acknowledged. We would like to thank Greg Valentine and Margaret Mangan for their constructive comments on the study, and for the help of two reviewers and Associate Editor Mark Bebbington in improving the presentation of the science.

Additional Files

Two additional files are available for download: `TableS1.xlsx, TableS2.xlsx`

These Excel workbook files contains the past ages and locations for volcanic eruptions in LVVR after 180 ka. Vent names have been matched to event ages. Subsets, States and the standard deviation of temporal uncertainty are reported. `TableS1.xlsx` contains the dataset adopted in the main text, while `TableS2.xlsx` contains the modified dataset adopted in Appendix B.

References

Achauer, U., Greene, L., Evans, J.R. & Lyer, H.M. (1986) Nature of the magma chamber underlying the Mono Craters area, eastern California, as determined from teleseismic traveltime residuals. *Journal of Geophysical Research: Solid Earth*, **91**(B14):13873–13891. DOI 10.1029/JB091iB14p13873. 5

Ajami, Newsha K, Duan, Qingyun & Sorooshian, Soroosh (2007) An integrated hydrologic Bayesian multimodel combination framework: Confronting input, parameter, and model structural uncertainty in hydrologic prediction. *Water Resources Research*, **43**(1). DOI 10.1029/2005WR004745. 4, 33

Aspinall, Willy P & Woo, Gordon (2014) Santorini unrest 2011–2012: an immediate Bayesian belief network analysis of eruption scenario probabilities for urgent decision support under uncertainty. *Journal of Applied Volcanology*, **3**(1):12. DOI 10.1186/s13617-014-0012-8. 4

Bailey, R.A. (1976) Volcanism, structure, and geochronology of the *longvalley* caldera, *monocounty*, *california*. *Journal of Geophysical Research: Solid Earth*, **81**(5):104–122. DOI 10.1029/JB081i005p00725. 5

Bailey, RA (1989) Geologic map of the Long Valley Caldera, Mono-Inyo Craters Volcanic Chain and vicinity, Eastern California, Misc. investigations series map I-1933. 1: 62,500. IMAP: i1933. 3, 5, 9, 10, 15, 24

Bartolini, S., Cappello, A., Martì, J. & Negro, C. Del (2013) Q-vast: A new quantum GIS plug-in for estimating volcanic susceptibility. *Natural Hazards and Earth System Sciences*, **13**:3031–3042. DOI 10.5194/nhess-13-3031-2013. 4

Bayarri, MJ, Berger, JO, Calder, ES, Patra, Abani K, Pitman, E Bruce, Spiller, Elaine T & Wolpert, Robert L (2015) Probabilistic quantification of hazards: A methodology using small ensembles of physics-based simulations and statistical surrogates. *International Journal for Uncertainty Quantification*, **5**(4):297–325. DOI 10.1615/Int.J.UncertaintyQuantification.2015011451. 24

Bayarri, MJ, Berger, James O, Calder, Eliza S, Dalbey, Keith, Lunagomez, Simon, Patra, Abani K, Pitman, E Bruce, Spiller, Elaine T & Wolpert, Robert L (2009) Using statistical and computer models to quantify volcanic hazards. *Technometrics*, **51**(4):402–413. DOI 10.1198/TECH.2009.08018. 24

Bebbington, Mark S (2013) Assessing spatio-temporal eruption forecasts in a monogenetic volcanic field. *Journal of Volcanology and Geothermal Research*, **252**:14–28. DOI 10.1016/j.jvolgeores.2012.11.010. 4

Bebbington, Mark S (2015) Spatio-volumetric hazard estimation in the Auckland volcanic field. *Bulletin of Volcanology*, **77**(5):39. DOI 10.1007/s00445-015-0921-3. 4, 13, 15

Bebbington, Mark S & Cronin, Shane J (2011) Spatio-temporal hazard estimation in the Auckland Volcanic Field, New Zealand, with a new event-order model. *Bulletin of Volcanology*, **73**(1):55–72. DOI 10.1007/s00445-010-0403-6. 4, 12, 13

Bergfeld, Deborah, Evans, William C., Howle, James F. & Hunt, Andrew G. (2015) Magmatic gas emissions at Holocene volcanic features near Mono Lake, California, and their relation to regional magmatism. *Journal of Volcanology and Geothermal Research*, **292**:70–83. 10.1016/j.jvolgeores.2015.01.008. 11

Bevilacqua, Andrea (2016) *Doubly stochastic models for volcanic hazard assessment at Campi Flegrei caldera, Theses*. Springer. ISBN 9788876425776. 4

Bevilacqua, Andrea, Flandoli, Franco, Neri, Augusto, Isaia, Roberto & Vitale, Stefano (2016) Temporal models for the episodic volcanism of Campi Flegrei caldera (Italy) with uncertainty quantification. *Journal of Geophysical Research: Solid Earth*, **121**(11):7821–7845. DOI 10.1002/2016JB013171. 4

Bevilacqua, Andrea, Isaia, Roberto, Neri, Augusto, Vitale, Stefano, Aspinall, Willy P, Bisson, Marina, Flandoli, Franco, Baxter, Peter J, Bertagnini, Antonella, Esposti Ongaro, Tomaso *et al.* (2015) Quantifying volcanic hazard at Campi Flegrei caldera (Italy) with uncertainty assessment: 1. vent opening maps. *Journal of Geophysical Research: Solid Earth*, **120**(4):2309–2329. DOI 10.1002/2014JB011775. 4, 12, 13, 17, 24

Browne, Brandon, Bursik, Marcus, Deming, Justin, Louros, Michael, Martos, Antonio & Stine, Scott (2010) Eruption chronology and petrologic reconstruction of the ca. 8500 yr B.P. eruption of Red Cones, southern Inyo chain, California. *Geological Society of America Bulletin*, **122**(9-10):1401–1422. DOI 10.1130/B30070.1. 2

Bursik, M (2009) A general model for tectonic control of magmatism: examples from Long Valley Caldera (USA) and El Chichón (México). *Geofísica Internacional*, **48**(1):171–183. ISSN 0016-7169. 2, 9

Bursik, Marcus & Sieh, Kerry (1989) Range front faulting and volcanism in the Mono Basin, eastern California. *Journal of Geophysical Research: Solid Earth*, **94**(B11):15587–15609. DOI 10.1029/JB094iB11p15587. 2, 5, 9, 10, 11, 15, 24

Bursik, Marcus & Sieh, Kerry (2013) Digital database of the Holocene tephras of the Mono-Inyo Craters, California. Data Series 758, US Geological Survey. URL. 2, 5, 7, 24

Bursik, Marcus, Sieh, Kerry & Meltzner, Aron (2014) Deposits of the most recent eruption in the Southern Mono Craters, California: description, interpretation and implications for regional marker tephras. *Journal of Volcanology and Geothermal Research*, **275**:114–131. DOI 10.1016/j.jvolgeores.2014.02.015. 5

Bursik, Marcus I & Gillespie, Alan R (1993) Late Pleistocene glaciation of Mono Basin, California. *Quaternary Research*, **39**(1):24–35. DOI 10.1006/qres.1993.1003. 34

Calais, Eric, d'Oreye, Nicolas, Albaric, Julie, Deschamps, Anne, Delvaux, Damien, Déverchere, Jacques, Ebinger, Cynthia, Ferdinand, Richard W, Kervyn, François, Macheyeki, Athanas S *et al.* (2008) Strain accommodation by slow slip and dyking in a youthful continental rift, East Africa. *Nature*, **456**(7223):783–787. DOI 10.1038/nature07478. 2

Cappello, Annalisa, Geshi, Nobuo, Neri, Marco & Del Negro, Ciro (2015) Lava flow hazards—an impending threat at Miyakejima volcano, Japan. *Journal of Volcanology and Geothermal Research*, **308**:1–9. DOI 10.1016/j.jvolgeores.2015.10.005. 12

Cappello, A, Neri, M, Acocella, V, Gallo, G, Vicari, A & Del Negro, C (2012) Spatial vent opening probability map of Etna volcano (Sicily, Italy). *Bulletin of Volcanology*, **74**(9):2083–2094. DOI 10.1007/s00445-012-0647-4. 4, 12

Chapman, N, Apted, M, Aspinall, W, Berryman, K, Cloos, M, Connor, C, Connor, L, Jaquet, O, Kiyosugi, K, Scourse, E *et al.* (2012) Topaz project: Long-term tectonic hazard to geological repositories - an extension of the itm probabilistic hazard assessment methodology to 1 myr. Report NUMO-TR-12-05, Nuclear Waste Management Organization of Japan (NUMO). PDF NUMO-TR-12-05. 12

Connor, Charles B & Hill, Brittain E (1995) Three nonhomogeneous Poisson models for the probability of basaltic volcanism: application to the Yucca Mountain region, Nevada. *Journal of Geophysical Research: Solid Earth*, **100**(B6):10107–10125. DOI 10.1029/95JB01055. 4, 11, 15

Connor, Charles B, Stamatakos, John A, Ferrill, David A, Hill, Brittain E, Ofoegbu, Goodluck I, Conway, F Michael, Sagar, Budhi & Trapp, John (2000) Geologic factors controlling patterns of small-volume basaltic volcanism: Application to a volcanic hazards assessment at Yucca Mountain, Nevada. *Journal of Geophysical Research: Solid Earth*, **105**(B1):417–432. DOI 10.1029/1999JB900353. 2, 11

Connor, Laura J, Connor, Charles B, Meliksetian, Khachatur & Savov, Ivan (2012) Probabilistic approach to modeling lava flow inundation: a lava flow hazard assessment for a nuclear facility in Armenia. *Journal of Applied Volcanology*, **1**(1):3. DOI 10.1186/2191-5040-1-3. 4, 12, 13

Cox, David Roxbee & Isham, Valerie (1980) *Point processes*, volume 12 of *Monographs on Statistics & Applied Probability*. Chapman and Hall/CRC Press. ISBN 9780412219108. 4

Daley, Daryl J & Vere-Jones, David (2005) *An Introduction to the Theory of Point Processes: Volume I: Elementary Theory and Methods*. Probability and Its Applications. Springer-Verlag, 2 edition. ISBN 0-387-95541-0. 4

Daley, Daryl J & Vere-Jones, David (2008) *An Introduction to the Theory of Point Processes: Volume II: General Theory and Structure*. Probability and Its Applications. Springer Science & Business Media. DOI 10.1007/978-0-387-49835-5. 4

Dalrymple, G Brent (1967) Potassium-argon ages of recent rhyolites of the Mono and Inyo Craters, California. *Earth and Planetary Science Letters*, **3**:289–298. DOI 10.1016/0012-821X(67)90050-7. 34

Duong, Tarn (2007) ks: Kernel density estimation and kernel discriminant analysis for multivariate data in R. *Journal of Statistical Software*, **21**(7):1–16. DOI 10.18637/jss.v021.i07. 4, 14

Duong, Tarn & Hazelton, Martin (2003) Plug-in bandwidth matrices for bivariate kernel density estimation. *Journal of Nonparametric Statistics*, **15**(1):17–30. DOI 10.1080/10485250306039. 4, 14

Eichelberger, John C, Vogel, Thomas A, Younker, Leland W, Miller, C Dan, Heiken, Grant H & Wohletz, Kenneth H (1988) Structure and stratigraphy beneath a young phreatic vent: South Inyo Crater, Long Valley caldera, California. *Journal of Geophysical Research: Solid Earth*, **93**(B11):13208–13220. DOI 10.1029/JB093iB11p13208. 11

Farrar, C. D., Sorey, M.L., Evans, W.C. & Howie, J.F. (1995) Forest-killing diffuse CO_2 emission at Mammoth Mountain as a sign of magmatic unrest. *Nature*, **376**(6542):675. DOI 10.1038/376675a0. 2, 5

Felpeto, Alicia, Martí, Joan & Ortiz, Ramon (2007) Automatic GIS-based system for volcanic hazard assessment. *Journal of Volcanology and Geothermal Research*, **166**(2):106–116. DOI 10.1016/j.jvolgeores.2007.07.008. 12

Gaffney, Edward S & Damjanac, Branko (2006) Localization of volcanic activity: topographic effects on dike propagation, eruption and conduit formation. *Geophysical Research Letters*, **33**(14). DOI 10.1029/2006GL026852. 11

Gaffney, Edward S, Damjanac, Branko & Valentine, Greg A (2007) Localization of volcanic activity: 2. effects of pre-existing structure. *Earth and Planetary Science Letters*, **263**(3):323–338. DOI 10.1016/j.epsl.2007.09.002. 2, 11

Gerlach, T. M., Doukas, M. P., McGee, K. A. & Kessler, R. (1999) Airborne detection of diffuse carbon dioxide emissions at Mammoth Mountain, California. *Geophysical Research Letters*, **26**(24):3661–3664. DOI 10.1029/1999GL008388. 2, 5

Gilbert, CM, Christensen, MN, Al-Rawi, Yehya & Lajoie, KR (1968) Structural and volcanic history of Mono basin, California-Nevada. *Geological Society of America Memoirs*, **116**:275–330. DOI 10.1130/MEM116-p275. 9

Hildreth, W. (2004) Volcanological perspectives on Long Valley, Mammoth Mountain, and Mono Craters: several contiguous but discrete systems. *Journal of Volcanology and Geothermal Research*, **136**(3–4):169–198. DOI 10.1016/j.jvolgeores.2004.05.019. 2, 3, 5, 10

Hildreth, Wes & Fierstein, Judy (2016) Eruptive history of Mammoth Mountain and its mafic periphery, California. Professional Paper 1812, US Geological Survey. DOI 10.3133/pp1812. 5, 7, 24, 26

Hildreth, W., Fierstein, J., Champion, D. & Calvert, A. (2014) Mammoth Mountain and its mafic periphery - a late Quaternary volcanic field in eastern California. *Geosphere*, **10**:1315–1365. DOI 10.1130/GES01053.1. 2, 5, 7, 26

Hildreth, Wes & Mahood, Gail A (1986) Ring-fracture eruption of the Bishop Tuff. *Geological Society of America Bulletin*, **97**(4):396–403. DOI 10.1130/0016-7606(1986)97<396:REOTBT>2.0.CO;2. 5, 9

Hill, David P (2006) Unrest in Long Valley Caldera, California, 1978–2004. *Geological Society, London, Special Publications*, **269**(1):1–24. DOI 10.1144/GSL.SP.2006.269.01.02. 2, 5, 11

Hill, David P (2017) Long Valley Caldera-Mammoth Mountain unrest: The knowns and the unknowns. *Elements*, **13**(1):8–9. DOI 10.2113/gselements.13.1.8. 5

Hill, David P, Mangan, Margaret T & McNutt, Stephen R (2017) Volcanic unrest and hazard communication in Long Valley Volcanic Region, California. *In* K. Nemeth (ed.) *Advances in Volcanology*, 1–17. Springer. DOI 10.1007/11157_2016_32. 5

Hill, David P & Montgomery-Brown, Emily (2015) Long Valley Caldera and the UCERF depiction of Sierra Nevada range-front faults. *Bulletin of the Seismological Society of America*. DOI 10.1785/0120150149. 9

Hincks, Thea K, Komorowski, Jean-Christophe, Sparks, Stephen R & Aspinall, Willy P (2014) Retrospective analysis of uncertain eruption precursors at La Soufrière volcano, Guadeloupe, 1975–77: volcanic hazard assessment using a bayesian belief network approach. *Journal of Applied Volcanology*, **3**(1):3. DOI 10.1186/2191-5040-3-3. 4

Hoeting, Jennifer A, Madigan, David, Raftery, Adrian E & Volinsky, Chris T (1999) Bayesian model averaging: a tutorial. *Statistical Science*, **14**(4):382–401. URL. 4, 33

Hu, Qiang, Smith, Patrick E, Evensen, Norman M & York, Derek (1994) Lasing in the Holocene: extending the $^{40}Ar/^{39}Ar$ laser probe method into the ^{14}C age range. *Earth and Planetary Science Letters*, **123**(1-3):331–336. DOI 10.1016/0012-821X(94)90277-1. 34

Huber, N King (1981) Amount and timing of late Cenozoic uplift and tilt of the central Sierra Nevada, California; evidence from the upper San Joaquin River basin. Professional Paper 1197, US Geological Survey. URL. 9

Jaquet, Olivier, Connor, Charles & Connor, Laura (2008) Probabilistic methodology for long-term assessment of volcanic hazards. *Nuclear Technology*, **163**(1):180–189. URL. 4

Jaquet, Olivier, Lantuéjoul, Christian & Goto, J (2012) Probabilistic estimation of long-term volcanic hazard with assimilation of geophysics and tectonic data. *Journal of Volcanology and Geothermal Research*, **235**:29–36. DOI 10.1016/j.jvolgeores.2012.05.003. 4, 12

Kiyosugi, Koji, Connor, Charles B, Wetmore, Paul H, Ferwerda, Brian P, Germa, Aurélie M, Connor, Laura J & Hintz, Amanda R (2012) Relationship between dike and volcanic conduit distribution in a highly eroded monogenetic volcanic field: San Rafael, Utah, USA. *Geology*, **40**(8):695–698. DOI 10.1130/G33074.1. 11

Le Corvec, Nicolas, Menand, Thierry & Lindsay, Jan (2013) Interaction of ascending magma with pre-existing crustal fractures in monogenetic basaltic volcanism: an experimental approach. *Journal of Geophysical Research: Solid Earth*, **118**(3):968–984. DOI 10.1002/jgrb.50142. 2, 11

Mader, H M, Coles, S G, Connor, C B & Connor, L J (eds.) (2006) *Statistics in Volcanology, Special publications of IAVCEI No. 1*. The Geological Society. ISBN 978-1-86239-208-3. 2

Magill, CR, McAneney, KJ & Smith, I EM (2005) Probabilistic assessment of vent locations for the next Auckland volcanic field event. *Mathematical Geology*, **37**(3):227–242. DOI 10.1007/s11004-005-1556-2. 9, 15

Marcaida, Mae (2015) *Resolving the Timing of Late Pleistocene Dome Emplacement at Mono Craters, California, from U–Th and Ar/Ar Dating*. Master's thesis, San Jose State University. URL. 34

Marti, Joan & Felpeto, Alicia (2010) Methodology for the computation of volcanic susceptibility: an example for mafic and felsic eruptions on Tenerife (Canary Islands). *Journal of Volcanology and Geothermal Research*, **195**(1):69–77. DOI 10.1016/j.jvolgeores.2010.06.008. 4

Martin, Andrew J, Umeda, Koji, Connor, Charles B, Weller, Jennifer N, Zhao, Dapeng & Takahashi, Masaki (2004) Modeling long-term volcanic hazards through Bayesian inference: An example from the Tohoku volcanic arc, Japan. *Journal of Geophysical Research: Solid Earth*, **109**(B10). DOI 10.1029/2004JB003201. 12, 15

Marzocchi, Warner & Bebbington, Mark S (2012) Probabilistic eruption forecasting at short and long time scales. *Bulletin of Volcanology*, **74**(8):1777–1805. DOI 10.1007/s00445-012-0633-x. 4

Marzocchi, Warner, Sandri, Laura, Gasparini, Paolo, Newhall, Christopher & Boschi, Enzo (2004) Quantifying probabilities of volcanic events: the example of volcanic hazard at Mount Vesuvius. *Journal of Geophysical Research: Solid Earth*, **109**(B11). DOI 10.1029/2004JB003155. 4

Mazzarini, Francesco, Keir, Derek & Isola, Ilaria (2013) Spatial relationship between earthquakes and volcanic vents in the central-northern Main Ethiopian Rift. *Journal of Volcanology and Geothermal Research*, **262**:123–133. DOI 10.1016/j.jvolgeores.2013.05.007. 13

Mazzarini, Francesco, Le Corvec, Nicolas, Isola, Ilaria & Favalli, Massimiliano (2016) Volcanic field elongation, vent distribution, and tectonic evolution of a continental rift: The Main Ethiopian Rift example. *Geosphere*, **12**(3):706–720. DOI 10.1130/GES01193.1. 11, 12

McGee, K.A. & Gerlach, T.M. (1998) Annual cycle of magmatic CO_2 in a tree-kill soil at Mammoth Mountain, California; implications for soil acidification. *Geology*, **26**(5):463–466. DOI 10.1130/0091-7613(1998)026<0463:ACOMCI>2.3.CO;2. 2, 5

Miller, C. Dan (1985) Holocene eruptions at the Inyo volcanic chain, California: Implications for possible eruptions in Long Valley caldera. *Geology*, **13**(1):14–17. DOI 10.1130/0091-7613(1985)13<14:HEATIV>2.0.CO;2. 5

Miller, C Dan, Mullineaux, DR, Crandell, DR & Bailey, RA (1982) Potential hazards from future volcanic eruptions in the Long Valley-Mono Lake area, east-central California and southwest Nevada; a preliminary assessment. Circular 877, US Geological Survey. URL. 2, 24

Neri, Augusto, Bevilacqua, Andrea, Esposti Ongaro, Tomaso, Isaia, Roberto, Aspinall, Willy P, Bisson, Marina, Flandoli, Franco, Baxter, Peter J, Bertagnini, Antonella, Iannuzzi, Enrico *et al.* (2015) Quantifying volcanic hazard at Campi Flegrei caldera (Italy) with uncertainty assessment: 2. pyroclastic density current invasion maps. *Journal of Geophysical Research: Solid Earth*, **120**(4):2330–2349. DOI 10.1002/2014JB011776. 4, 24

Peacock, Jared R, Mangan, Margaret T, McPhee, D & Ponce, David A (2015) Imaging the magmatic system of Mono Basin, California, with magnetotellurics in three dimensions. *Journal of Geophysical Research: Solid Earth*, **120**(11):7273–7289. DOI 10.1002/2015JB012071. 5

Peacock, J. R., Mangan, M. T., McPhee, D. & Wannamaker, P. E. (2016) Three-dimensional electrical resistivity model of the hydrothermal system in Long Valley Caldera, California, from magnetotellurics. *Geophysical Research Letters*, **43**(15):7953–7962. DOI 10.1002/2016GL069263. 2, 5

Prejean, Stephanie, Stork, Anna, Ellsworth, William, Hill, David & Julian, Bruce (2003) High precision earthquake locations reveal seismogenic structure beneath Mammoth Mountain, California. *Geophysical Research Letters*, **30**(24):2247. DOI 10.1029/2003GL018334. 5

Reches, Ze'ev & Fink, Jonathan H (1988) The mechanism of intrusion of the Inyo dike, Long Valley Caldera, California. *Journal of Geophysical Research: Solid Earth*, 4321–4334. DOI 10.1029/JB093iB05p04321. 11

Reid, Mary R (2003) New ages for young rhyolites, Mono Craters, California: Ion microprobing into the Holocene. *In Abstracts with Programs*, volume 35. GSA Seattle Annual Meeting, Geological Society of America, Seattle, Washington (USA). Abstract 67515. 34

Rougier, Jonathan, Hill, Lisa J, Sparks, Steve & Sparks, Robert Stephen John (eds.) (2013) *Risk and Uncertainty Assessment for Natural Hazards*. Cambridge University Press. ISBN 9781107310766. 2

Sandri, Laura, Costa, Antonio, Selva, Jacopo, Tonini, Roberto, Macedonio, Giovanni, Folch, Arnau & Sulpizio, Roberto (2016) Beyond eruptive scenarios: assessing tephra fallout hazard from Neapolitan volcanoes. *Scientific Reports*, **6**(24271). DOI 10.1038/srep24271. 24

Selva, Jacopo, Orsi, Giovanni, Di Vito, Mauro Antonio, Marzocchi, Warner & Sandri, Laura (2012) Probability hazard map for future vent opening at the Campi Flegrei caldera, Italy. *Bulletin of Volcanology*, **74**(2):497–510. DOI 10.1007/s00445-011-0528-2. 4, 12

Shelly, David R. & Hill, David P. (2011) Migrating swarms of brittle-failure earthquakes in the lower crust beneath Mammoth Mountain, California. *Geophysical Research Letters*, **38**(20):L20307. DOI 10.1029/2011GL049336. 5

Shelly, David R., Taira, Taka'aki, Prejean, Stephanie G., Hill, David P. & Dreger, Douglas S. (2015) Fluid-faulting interactions: Fracture-mesh and fault-valve behavior in the February 2014 Mammoth Mountain, California, earthquake swarm. *Geophysical Research Letters*, **42**(14):5803–5812. DOI 10.1002/2015GL064325. 5

Sieh, Kerry & Bursik, Marcus (1986) Most recent eruption of the Mono Craters, eastern central California. *Journal of Geophysical Research: Solid Earth*, **91**(B12):12539–12571. DOI 10.1029/JB091iB12p12539. 5

Sparks, RSJ & Aspinall, WP (2004) Volcanic activity: frontiers and challenges in forecasting, prediction and risk assessment. *In* R. Sparks & C. Hawkesworth (eds.) *The State of the Planet: Frontiers and Challenges in Geophysics*, volume 150 of *Geophysical Monograph Series*, 359–373. American Geophysical Union. ISBN 9781118666012. DOI 10.1029/GM150. 4

Steel, Mark FJ (2011) Bayesian model averaging and forecasting. *Bulletin of EU and US Inflation and Macroeconomic Analysis*, **200**(Special issue):30–41. ISSN 1888-9298. 4, 33

Vegas, N, Aranguren, A & Tubía, JM (2001) Granites built by sheeting in a fault stepover (the Sanabria Massifs, Variscan Orogen, NW Spain). *Terra Nova*, **13**(3):180–187. DOI 10.1046/j.1365-3121.2001.00343.x. 9

Vere-Jones, David (1992) Statistical methods for the description and display of earthquake catalogues. *In* A.T. Walden & P. Guttorp (eds.) *Statistics in the Environmental and Earth Sciences*. Hodder Education Publishers. ISBN 9780340545300. 4, 15

Volentik, Alain CM & Houghton, Bruce F (2015) Tephra fallout hazards at Quito International Airport (Ecuador). *Bulletin of Volcanology*, **77**(6):50. DOI 10.1007/s00445-015-0923-1. 24

Woo, Gordon (1999) *The Mathematics of natural catastrophes*. World Scientific. ISBN 9781783261970 (ebook). 2

Yan, Hongxiang & Moradkhani, Hamid (2016) Toward more robust extreme flood prediction by bayesian hierarchical and multimodeling. *Natural Hazards*, **81**(1):203–225. DOI 10.1007/s11069-015-2070-6. 4, 33

Yang, Qingyuan & Bursik, Marcus (2016) A new interpolation method to model thickness, isopachs, extent, and volume of tephra fall deposits. *Bulletin of Volcanology*, **78**(10):68. DOI 10.1007/s00445-016-1061-0. 5, 34

Appendix A: Bayesian model averaging

This appendix describes additional technical details on the vent propagation distance estimator and on the model averaging procedure. In general, the Bayesian model averaging (BMA) provides a coherent mechanism for weighted averaging of alternative models, allowing the production of more comprehensive output estimates (*Hoeting et al.*, 1999; *Ajami et al.*, 2007; *Steel*, 2011; *Yan & Moradkhani*, 2016).

Let $(M_i), i = 1, ..., n$ be a set of alternative probability models for the calculation of a random quantitative output δ, such that we do not know which is the correct one. The main step of BMA is to define some scores $s(i), i = 1, ..., n$ for the models based on a set of available observations (D) about the quantity δ. The scores are normalized to sum to one, allowing the definition of a discrete probability distribution on the models set $(M_i), i = 1, ..., n$. These scores represent the probability of the models to be correct, assuming that exactly one of them is correct. Equal prior scores, $s(i), i = 1, ..., n$, are assumed for each model, such that $s_i = \frac{1}{n} \, \forall \, i$. Bayes Theorem states that, for each $i = 1, ..., n$, the posterior weights can be calculated as:

$$s(i|D) = \frac{L_i(D) \cdot s(i)}{C}, \tag{11}$$

where L_i is the likelihood associated to model i, and C is a normalizing constant such that the posterior weights sum to one. Hence, starting from equal prior scores, the posterior scores are proportional to the likelihoods of observed data. A maximum likelihood approach would have considered only the best fitting model, while the BMA's more conservative approach allows a weighted average of all models.

In this study there are two outputs (δ) on which BMA is applied: one is the propagation distance (d) of each new vent from the cluster of previously active vents, according to the model set $(M_i), i = 1, ..., 7$, where model M_i uses the propagation distance of the vent from the i^{th} spatially closest of the previously active vents, and the other is the vent opening location $\mathbf{X}$, according to the model set $(M_i), i = 1, 2, 3$, where M_1 is the kernel density estimation model, M_2 is the model based on the Bayesian update of the fault map, and M_3 the uniformly distributed probability map. In both the cases, the observations inside D are generated through a hind-casting validation technique set up for each of the most recently active vents.

Distance of propagation. In this case the set D includes $m = 25$ elements for State A (post 93 ka) and for State B (post 3.5 ka). In detail, for each model (M_j) the total likelihood $(L_j(D))$ is the product of the likelihoods of the considered events:

$$s(j|D) = \frac{1}{Cn} \prod_{i=1}^{m} \int_{D_i} f_j^i(\mathbf{x}) d\mathbf{x}, \tag{12}$$

where C is a normalizing constant, n is the number of models, f_j^i is the density of the vent location model obtained restricting k_A and k_B, respectively, to the vents active before the i^{th} and calculating d according to the model M_j. The same scores concern all the observations inside D.

Vent opening models. In this case each one of the $m = 25$ most recent events is separately selected as a potential observation (*i.e.,* the site of the disk of uncertainty D_i, for i in $1, \ldots, m$. Hence, m different triplets of posterior scores are calculated. This permits the assumption of changing scores as a function of the event. A statistic of the total likelihood is defined as the average of such values, according to the expression:

$$\overline{s(j|D_i)}_{i=1,\ldots,m} = \frac{C}{mn} \sum_{i=1}^{m} \int_{D_i} f_j^i(\mathbf{x}) d\mathbf{x}, \tag{13}$$

where f_j^i is the density of the j^{th} vent location model obtained restricting k (for M_1 and M_2) to the vents active before the i^{th}. This average is the estimator for the scores adopted in the averaged model for calculating the vent opening probability map in LVVR.

Appendix B: Effects of an eruptive record change

The eruptive record of the LVVR region is the subject of ongoing research (*Yang & Bursik*, 2016), and the age of several events could be constrained differently by newer measurements. In addition, some vent locations have not yet been dated; these are displayed with small purple dots in Figure 1, together with the vents older than 180 ka. The availability of additional information and the update of the eruption record will also affect the BMA procedure, potentially changing the scores of the models in a way that improves the multi-model performance. This section provides an example of eruptive record change, concerning the [2−50] ka time interval, according with other radio-isotopic dates reported in literature (*Dalrymple*, 1967; *Bursik & Gillespie*, 1993; *Hu et al.*, 1994; *Reid*, 2003; *Marcaida*, 2015). The alternative record is reported in the additional file *TableS2.xlsx*.

Figure 12a shows the cumulative plot of this alternative eruption record. Main differences affect the Mono domes sequence, which is assumed to be older and re-ordered. Moreover, the State B first event is now dated at 42.5 ka instead of 59.4 ka. Modifications in Subsets 3A, 3B and the initial part of 4 change the observed propagation distances, with non-negligible effects noticed only on the Model 1 results. They do not produce significant effects on Model 2 and 3 results. The new Bayesian model averaging scores for propagation distance are presented in Table 3.

Table 3: The BMA weights, bandwidth selection for Model 1 (alternative record for State B)

Scores	$\mathbf{M}_1$	$\mathbf{M}_2$	$\mathbf{M}_3$	M_4	M_5	M_6	M_7
State B (s^B)	0.00%	0.00%	0.59%	96.25%	0.25%	2.58%	0.34%

Figure 12*b* shows the output of the new posterior kernel function, which appears more diffuse than before the record change. This change affects the vent opening probability map, shown in Figure 12**c**. The probability of vent opening in the Mono region is slightly less peaked than the probability shown in Figure 7. The maximum probability value decreases 0.5% per km^2 because the same amount of probability is spread over a larger area.

Model performance appears to not be significantly different after the dataset change. The new BMA weights are presented in Table 4.

Table 4: The BMA weights for multiple models.

Scores	**5^{th} percentile**	**mean**	**95^{th} percentile**
Model 1 (q_1)	34.82%	**39.38%**	46.15%
Model 2 (q_2)	45.52%	**51.88%**	56.09%
Model 3 (q_3)	07.04%	**08.74%**	11.07%

Figure 13 presents the probability maps: (a) 5^{th} percentile values, (b) mean values, and (c) 95^{th} percentile values. Again, the results are not significantly different from those in Figure 10, showing only a minor reduction of the Mono maximum. The averaged model results prove to be quite robust against the described change in the eruption record.

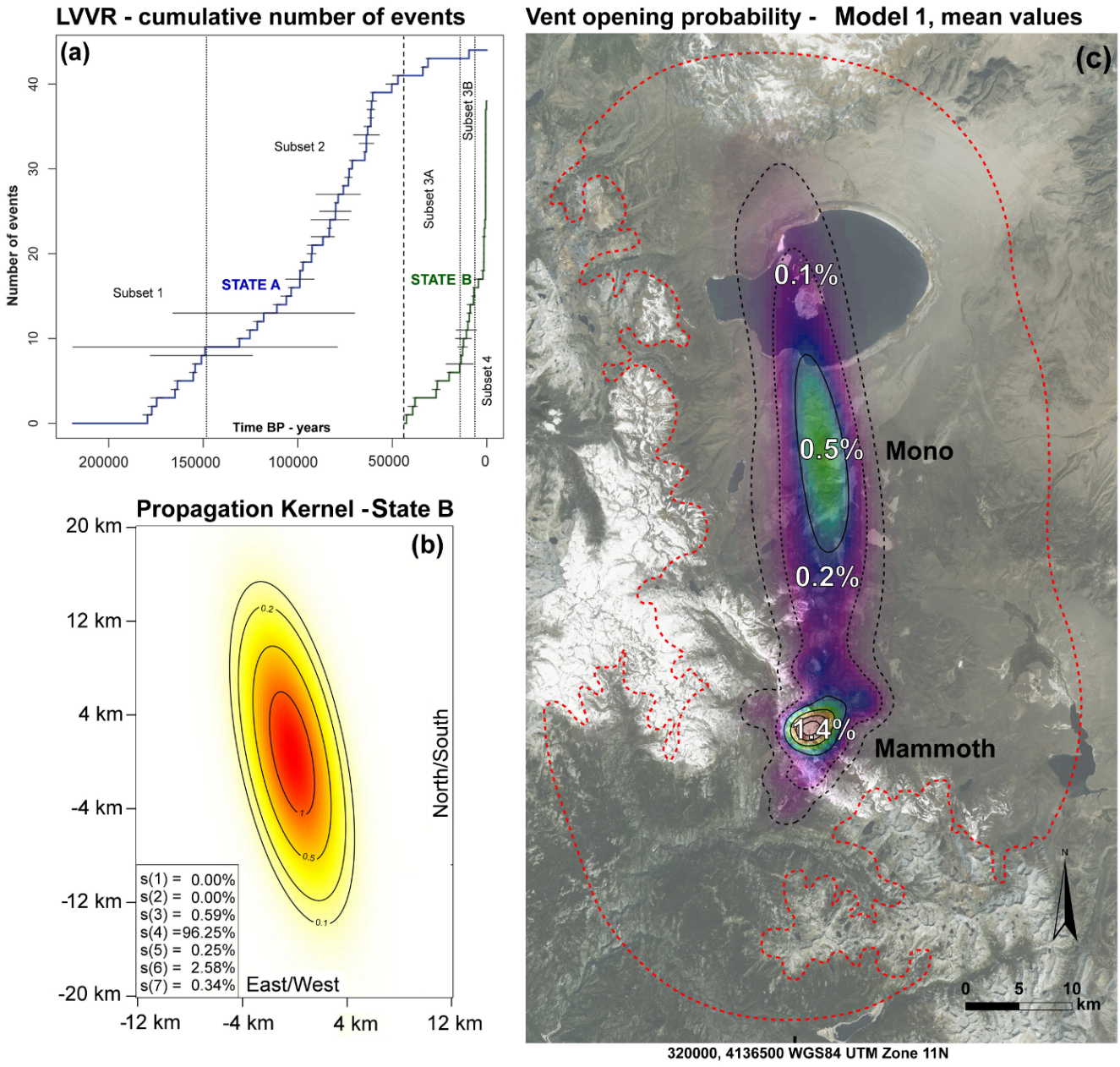

Figure 12: (a) Cumulative number of past events as a function of time according to the changed eruption record. Vertical lines separate subsets. The blue and green curves separate States A and B. Horizontal segments display preliminary age uncertainty. (b) Plots of the new kernel posterior distribution. Frame presents the posterior weights. (c) Spatial vent opening probability map for LVVR based on kernel density estimation method and changed record. In (b-c) colors, contours and values describe probability as a percentage per km^2. Black lines are 0.3% spaced, dashed lines mark 0.1% and 0.02% probability density levels. Red dashed line marks the map boundary.

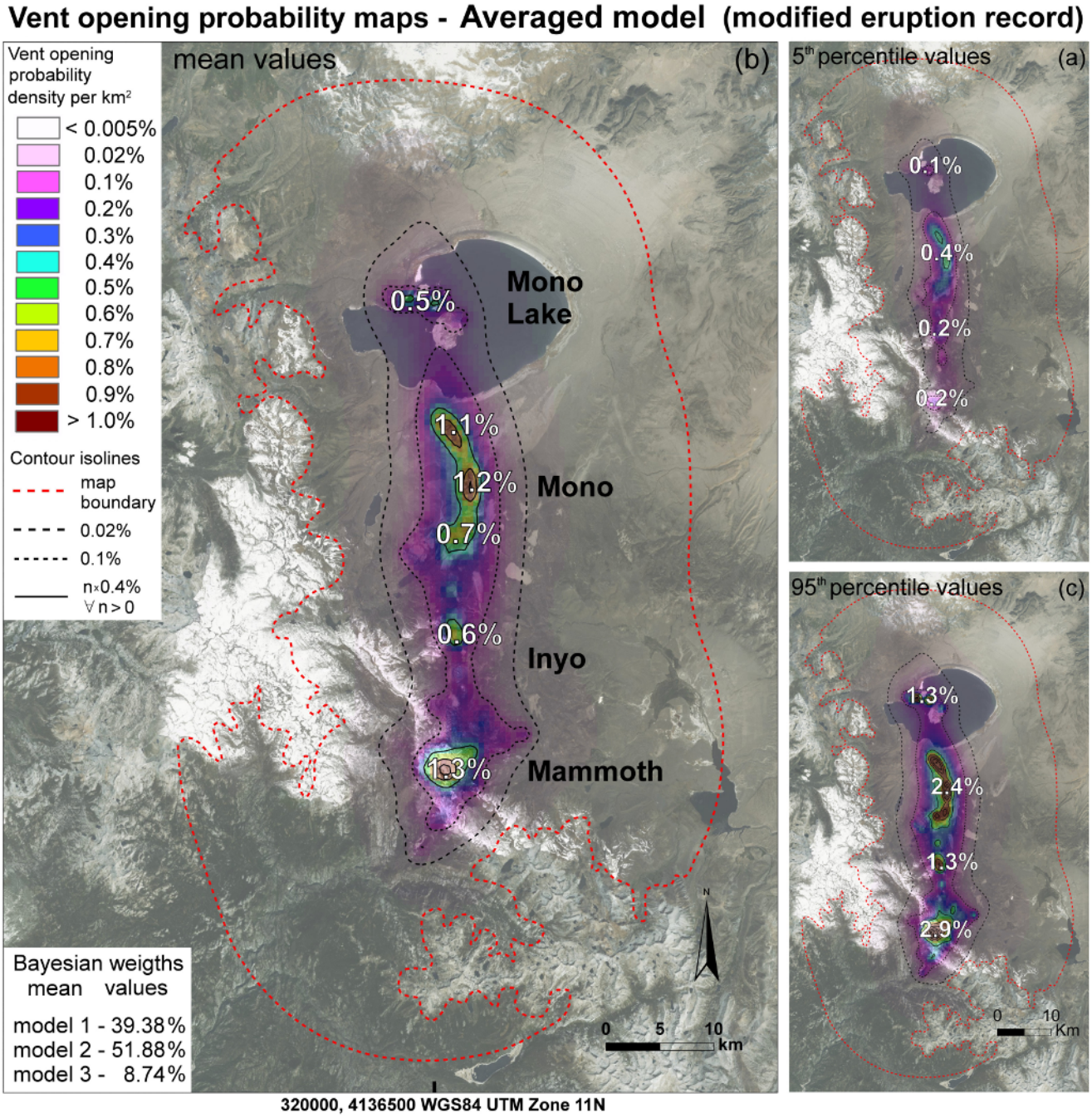

Figure 13: Spatial vent opening probability maps for LVVR based on three integrated models (BMA) and the changed record. (a) shows the 5^{th} percentile values, (b) the mean values, and (c) the 95^{th} percentile values of probability. Color, contours and numbers describe probability as a percentage per km^2. Black lines are 0.4% spaced, dashed lines mark 0.1% and 0.02% probability density levels. Red dashed line marks the map boundary.